



## Ultrafast four-wave-mixing spectroscopy with two vacuum fields and coincidence-double-heterodyne detection

HARI KUMAR YADALAM,<sup>1,2,3</sup>  MATTHIAS KIZMANN,<sup>1,2,4</sup>  AND SHAUL MUKAMEL<sup>1,2,5</sup>

<sup>1</sup>Department of Chemistry, University of California, Irvine, California 92614, USA

<sup>2</sup>Department of Physics and Astronomy, University of California, Irvine, California 92614, USA

<sup>3</sup>hyadalam@uci.edu

<sup>4</sup>mkizmann@uci.edu

<sup>5</sup>smukamel@uci.edu

Received 21 March 2024; revised 4 August 2024; accepted 26 August 2024; published 2 October 2024

**In classical macroscopic ultrafast optical four-wave mixing signals, phase matching selects three classes of light–matter interaction pathways: double quantum coherence; non-rephasing; and photon-echo. Multiple pathways contribute to each of these signals. We show that a coincidence-double-heterodyne detection scheme that employs two classical and two vacuum fields can isolate a single pathway contribution to each of these signals. We further demonstrate the advantage of the proposed technique by comparing it with the classical photon-echo signal for a model Frenkel-exciton dimer.**

© 2024 Optica Publishing Group under the terms of the [Optica Open Access Publishing Agreement](#)

<https://doi.org/10.1364/OPTICAQ.523848>

### 1. INTRODUCTION

Femtosecond optical four-wave mixing signals are commonly used for probing electronic and nuclear dynamics [1–7]. These are usually performed with heterodyne detection [1]. Three pulses interact with the sample to create a nonlinear polarization, while the fourth, reference, pulse acts as a local oscillator. The induced polarization generates a pulse in the same direction as the fourth pulse and is heterodyne detected with it. For macroscopic samples, signals from many molecules interfere destructively in most directions, except in the phase matching directions, where they constructively interfere [1,3,6,7]. Standard four-wave mixing spectroscopies have three dominant phase matching directions:  $\mathbf{k}_4 = -\mathbf{k}_3 + \mathbf{k}_2 + \mathbf{k}_1$  (double quantum coherence);  $\mathbf{k}_4 = \mathbf{k}_3 - \mathbf{k}_2 + \mathbf{k}_1$  (non-rephasing); and  $\mathbf{k}_4 = \mathbf{k}_3 + \mathbf{k}_2 - \mathbf{k}_1$  (photon echo) [1,3,6,7]. Each selects its own class of pathways represented by ladder diagrams. The appearance of multiple pathways complicates the interpretation of these signals and further pathway selectivity is highly desirable.

Over the past decade, nonlinear spectroscopies which combine quantum light and quantum interferometry were proposed for achieving better resolution at low intensities of input fields [8–23]. Due to the back-action of the material systems on the quantum states of light, the light–matter interaction sequence is distinct compared with those in classical nonlinear spectroscopies [24–26]. Interferometric techniques have been proposed for selectively probing pathways contributing to various nonlinear spectroscopies [27–33]. This selectivity is not possible with traditional spectroscopies which employ classical light and only detect a single outgoing field. Detecting several outgoing

fields rather than a single one can distinguish and isolate these pathways [30–33]. Selective probing of general multipoint correlation functions in a platform independent manner was discussed in Ref. [34].

Here, we show how a coincidence double-heterodyne detection scheme that employs classical coherent states and vacuum fields of light can achieve pathway selectivity in photon-echo signals. Pathway selectivity for other four-wave mixing signals is discussed in [Supplement 1](#).

### 2. COINCIDENCE DOUBLE-HETERODYNE DETECTION

Four-wave mixing signals are described by several ladder diagrams. Measuring the signals in different phase-matching directions with heterodyne detection can achieve some pathway selectivity. For example, the photon-echo signal is generated in the phase matching direction  $\mathbf{k}_4 = \mathbf{k}_3 + \mathbf{k}_2 - \mathbf{k}_1$ , and has the three contributing pathways shown in Fig. 1. To achieve further selectivity, we propose a coincidence detection scheme, which can select a single ladder diagram (along with its disconnected component) as shown in Fig. 2. We demonstrate this pathway selectivity for the photon-echo signal. Pathway selectivity in other phase-matching directions (non-rephasing and double quantum coherence signals) is discussed in [Supplement 1](#).

The proposed coincidence detection setup for the quantum light generated at the sample, Fig. 3, selects a single ladder diagram for each phase-matching direction. Our setup uses four ultrashort pulses. The first two, 1 and 2, with the wave vectors

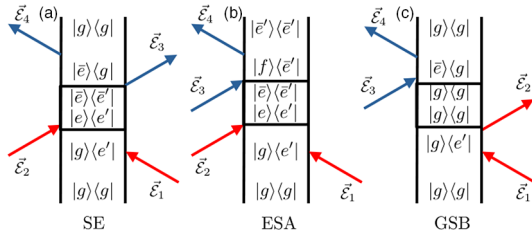


**Fig. 1.** Ladder diagrams contributing to the classical-heterodyne-detected photon-echo signal: SE, stimulated emission; ESA, excited state absorption; GSB, ground state bleach. The ladder diagrams shown here are shorthand descriptions of various light–matter interaction pathways [1]. The rules for interpreting such diagrams are detailed in Supplement 1. In these diagrams, the two vertical dark strands correspond to the ket and bra of the sample–field joint density matrix. Time flows from the bottom to the top. Within the rotating wave approximation for the sample–field interaction, inward (outward) pointing arrows at a specific time correspond to excitation (de-excitation) of the sample accompanied by absorption (emission) of photons from (into) the indicated laser pulse. During the interval between the two arrows, i.e., between two sample–field interaction events, the sample and field degrees of freedom evolve independently.

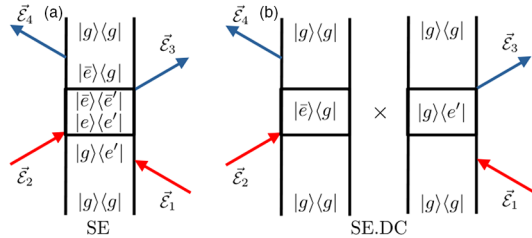


**Fig. 2.** Ladder diagrams contributing to the proposed double-heterodyne detected photon-echo signal. The diagram SE shown in panel (a) is selectively isolated by the proposed signal. As a consequence of translational averaging, the disconnected diagram SE,DC, shown in panel (b), has to be subtracted from the connected diagram SE, shown in panel (a), to obtain the macroscopic signal.

and polarizations  $\mathbf{k}_1$  and  $\mathbf{k}_2$ ,  $\epsilon_1$  and  $\epsilon_2$ , respectively, in coherent states are sent through the sample; as shown by the red lines in Fig. 3. The other two photon modes denoted 3 and 4 with the central wave vectors and polarizations  $\mathbf{k}_3$  and  $\mathbf{k}_4$ ,  $\epsilon_3$  and  $\epsilon_4$ , respectively, are initially in their vacuum state. Photons generated in these modes by the sample are represented by the dotted blue (before interacting with the sample) and solid blue (after interacting with the sample) lines in Fig. 3. The detectors in Fig. 3 select the wave vectors of these pulses. Hence, the central wave vectors,  $\mathbf{k}_1$  and  $\mathbf{k}_2$ , are controlled by the propagation directions of the incoming pulses. In contrast, the central wave vectors of the outgoing pulses from the sample,  $\mathbf{k}_3$  and  $\mathbf{k}_4$ , are selected by the detection system. A finite signal can only be observed when all the wave vectors satisfy one of the three phase-matching conditions. In the photon-echo signal, the wave vectors must satisfy  $\mathbf{k}_4 - \mathbf{k}_3 = \mathbf{k}_2 - \mathbf{k}_1$ . Each of the generated pulses 3 and 4 is mixed with its respective local oscillator,  $\tilde{3}$  and  $\tilde{4}$ , at the 50 : 50 beam splitters, as shown in Fig. 3. Note that, these local oscillators do not pass through the sample, unlike the classical signal which only involves a single local oscillator. Finally, two heterodyne measurements are performed in

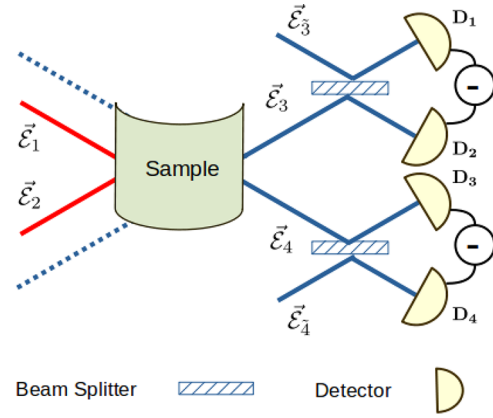


**Fig. 3.** Proposed coincidence double-heterodyne detection scheme for selecting pathways contributing to four-wave mixing spectroscopies. In this scheme, two incoming pulses (1 and 2), initially prepared in coherent states, interact with the sample. The sample generates photons in the modes 3 and 4, initially in their vacuum. Thus, generated pulses at the sample are mixed with reference pulses,  $\tilde{3}$  and  $\tilde{4}$ , prepared in coherent states at the two beam splitters. The detectors select the wave vector directions of outgoing modes from the sample, 3 and 4. The proposed signal involves coincident detection of these two heterodyne measurements.

coincidence to generate the signal,

$$\mathcal{S} = \langle : (I_{D_1} - I_{D_2})(I_{D_3} - I_{D_4}) : \rangle, \quad (1)$$

where  $I_{D_n}$  is the time-integrated electric field intensity operator at the  $D_n$  detector, given by the following Liouville space superoperator expression:

$$I_{D_n} = \frac{1}{2\pi c_n^2} \int_{-\infty}^{+\infty} dt \tilde{\mathcal{E}}_{D_n R}^\dagger(t) \cdot \tilde{\mathcal{E}}_{D_n L}(t),$$

where  $\tilde{\mathcal{E}}_{D_n}$  is the positive frequency component of the electric field operator at the  $D_n$  detector. The  $L/R$  indices are left/right Liouville space superoperator indices defined below. The  $c_n$ , defined below, is a constant that depends on the transverse area of the pulses and their central frequencies. We note that the normal ordering of Hilbert space operators as implied by the symbol  $: \dots :$  in the above coincidence signal, is automatically accounted for by expressing the field operators in terms of Liouville space operators [8]. Expressing the electric field operators at the detectors in terms of the field operators at the input ports of the 50 : 50 beam splitters gives the following expressions for the differential intensity at pairs of detectors ( $D_1 - D_2$  and  $D_3 - D_4$ ):

$$I_{D_1} - I_{D_2} = \frac{i}{2\pi c_3 c_3} \int_{-\infty}^{+\infty} dt \langle [\tilde{\mathcal{E}}_{3R}^\dagger(t) \cdot \tilde{\mathcal{E}}_{3L}(t) - \tilde{\mathcal{E}}_{3R}^\dagger(t) \cdot \tilde{\mathcal{E}}_{3L}(t)] \rangle,$$

$$I_{D_3} - I_{D_4} = \frac{-i}{2\pi c_4 c_4} \int_{-\infty}^{+\infty} dt \langle [\tilde{\mathcal{E}}_{4R}^\dagger(t) \cdot \tilde{\mathcal{E}}_{4L}(t) - \tilde{\mathcal{E}}_{4R}^\dagger(t) \cdot \tilde{\mathcal{E}}_{4L}(t)] \rangle, \quad (4)$$

where  $\tilde{\mathcal{E}}_n$  is the positive frequency component of the electric field operator of the  $n$ th pulse. Hence, in the above signal,  $\mathcal{S}$ , the two terms,  $(I_{D_1} - I_{D_2})$  and  $(I_{D_3} - I_{D_4})$ , correspond, respectively, to the product of electric field amplitudes of pulses 3 (generated at the sample), and  $\tilde{3}$  (its reference local oscillator); and pulses 4 (generated at the sample) and  $\tilde{4}$  (its reference local oscillator). These individual measurements are

analogous to the standard-heterodyne detection, which probes coherence between two fields. As in the proposed signal, these two heterodyne measurements are performed in coincidence; we refer to it as the coincidence-double-heterodyne detection signal. This signal is analogous to the one proposed in Ref. [31]. Here,  $\mathcal{S}$ , depends on polarizations, wave vectors, and temporal profiles of the four pulses 1, 2,  $\tilde{3}$ ,  $\tilde{4}$ . Hereafter, we shall fix the polarizations and wave vectors of these pulses and vary the three time delays between the four pulses.

The four pulses,  $\mathcal{I} = 1, 2, \tilde{3}, \tilde{4}$ , are initially in coherent states,

$$|\Psi(-\infty)\rangle = e^{\sum_{i \in \mathcal{I}} \int_{-\infty}^{+\infty} \frac{d\omega}{2\pi} [\alpha_i(\omega) a_{i\epsilon_i}^\dagger(\omega) - \alpha_i^*(\omega) a_{i\epsilon_i}(\omega)]} |\emptyset\rangle, \quad (5)$$

where  $a_{i\epsilon_i}^\dagger(\omega)$  is a bosonic creation operator for creating a photon in the pulse “ $i$ ” with frequency  $\omega$ , central wave vector  $\mathbf{k}_i$ , and polarization  $\epsilon_i$ . Here,  $|\emptyset\rangle$  represents the vacuum state of the field.

The Hamiltonian of the sample (a collection of non-interacting identical molecules), the light, and their interaction is

$$H = H_s + H_f + H_{sf},$$

$$H_f = \sum_{i \in \mathcal{I}} \sum_{\epsilon_i} \int_{-\infty}^{+\infty} d\omega \hbar \omega a_{i\epsilon_i}^\dagger(\omega) a_{i\epsilon_i}(\omega),$$

$$\mathcal{I} = 1, 2, 3, 4, \tilde{3}, \tilde{4},$$

$$\begin{aligned} S_{\mathcal{DH}} &= \left[ \prod_{i=3,4} \frac{1}{2\pi c_i c_i} \right] \int_{-\infty}^{+\infty} \int_{-\infty}^{+\infty} dt_4 dt_3 \langle \mathcal{T} \left[ \vec{\mathcal{E}}_{4R}^\dagger(t_4) \cdot \vec{\mathcal{E}}_{4L}(t_4) - \vec{\mathcal{E}}_{4R}^\dagger(t_4) \cdot \vec{\mathcal{E}}_{4L}(t_4) \right] \left[ \vec{\mathcal{E}}_{3R}^\dagger(t_3) \cdot \vec{\mathcal{E}}_{3L}(t_3) - \vec{\mathcal{E}}_{3R}^\dagger(t_3) \cdot \vec{\mathcal{E}}_{3L}(t_3) \right] \rangle \\ &= 2 \left[ \prod_{i=3,4} \frac{1}{2\pi c_i c_i} \right] \text{Re} \int_{-\infty}^{+\infty} \int_{-\infty}^{+\infty} dt_4 dt_3 \left[ \langle \mathcal{T} \vec{\mathcal{E}}_{4R}^\dagger(t_4) \cdot \vec{\mathcal{E}}_{4L}(t_4) \vec{\mathcal{E}}_{3R}^\dagger(t_3) \cdot \vec{\mathcal{E}}_{3L}(t_3) \rangle - \langle \mathcal{T} \vec{\mathcal{E}}_{4R}^\dagger(t_4) \cdot \vec{\mathcal{E}}_{4L}(t_4) \vec{\mathcal{E}}_{3R}^\dagger(t_3) \cdot \vec{\mathcal{E}}_{3L}(t_3) \rangle \right]. \end{aligned} \quad (10)$$

In the above equation, the second line is obtained from the first by expanding the square brackets in its integrand, which gives the sum of two terms and their complex conjugates. Combining these gives the real part of the two terms retained in the second line. Here the electric field operators are given in the interaction picture and  $\langle \mathcal{T} \dots \rangle = \text{Tr} \left[ \mathcal{T} \dots e^{-\frac{i}{\hbar} \int_{-\infty}^{+\infty} dt H_{sf}(t)} \rho(-\infty) \right]$ . The joint sample–field initial density matrix is given by  $\rho(-\infty) = \rho_s(-\infty) \otimes |\Psi(-\infty)\rangle \langle \Psi(-\infty)|$ , where  $\rho_s(-\infty) = \otimes_{n \in \text{sample}} |g\rangle_n \langle g|$  is the initial ground state of the sample and  $|\Psi(-\infty)\rangle$  is the initial field state defined in Eq. (5). Throughout this work, we use the superoperator notation:  $\mathcal{O}_L X = \mathcal{O} X$ ,  $\mathcal{O}_R X = X \mathcal{O}$ ,  $\mathcal{O}_- = \mathcal{O}_L - \mathcal{O}_R$ , and  $\mathcal{O}_+ = \frac{\mathcal{O}_L + \mathcal{O}_R}{2}$  [35,36]. A detection scheme analogous to the above signal was used in Refs. [37,38].

$$S_{\mathcal{DH}} = 2 \left[ \prod_{i=3,4} \frac{1}{2\pi c_i c_i} \right] \text{Re} \int_{-\infty}^{+\infty} \int_{-\infty}^{+\infty} dt_4 dt_3 \left[ \langle \mathcal{T} \vec{\mathcal{E}}_4^\dagger(t_4) \cdot \vec{\mathcal{E}}_{4L}(t_4) \vec{\mathcal{E}}_3^\dagger(t_3) \cdot \vec{\mathcal{E}}_{3L}(t_3) \rangle - \langle \mathcal{T} \vec{\mathcal{E}}_4^\dagger(t_4) \cdot \vec{\mathcal{E}}_{4L}(t_4) \vec{\mathcal{E}}_{3R}^\dagger(t_3) \cdot \vec{\mathcal{E}}_{3L}(t_3) \rangle \right], \quad (11)$$

where  $\vec{\mathcal{E}}_i(t_i) = \langle \Psi(-\infty) | \vec{\mathcal{E}}_i(t_i) | \Psi(-\infty) \rangle$  is the classical field envelope of the pulse “ $i$ ”.

In Eq. (11), the first term corresponds to measuring the anomalous correlation function of the entangled photons in pulses 3 and 4 generated at the sample, and the second term corresponds to measuring the coherence between photons in pulses 3 and 4 generated at the sample. In the first process, the sample, with its  $\chi^{(3)}$

$$H_{sf} = \int_{\text{sample}} d^3 \mathbf{r} \sum_{i=1}^4 \left[ e^{-i\mathbf{k}_i \cdot \mathbf{r}} \vec{\mathcal{E}}_i^\dagger \cdot \vec{\mathcal{V}}(\mathbf{r}) + e^{i\mathbf{k}_i \cdot \mathbf{r}} \vec{\mathcal{V}}(\mathbf{r}) \cdot \vec{\mathcal{E}}_i \right]. \quad (9)$$

Here the positive frequency component of the electric field operator for the pulse “ $i$ ,” with central wave vector,  $\mathbf{k}_i$ , frequency,  $\tilde{\omega}_i$ , and the transverse area  $A$ , at the sample is  $\vec{\mathcal{E}}_i = i c_i \sum_{\epsilon_i} \epsilon_i \int_{-\infty}^{+\infty} d\omega a_{i\epsilon_i}(\omega) \left( c_i = \sqrt{\frac{\hbar \tilde{\omega}_i}{4\pi \epsilon_0 c_0 A}} \right)$ . We assume that the frequency bandwidths of the pulses are much smaller than their respective central frequencies. Free space diffraction of the waves is neglected. For dilute samples, the sample Hamiltonian is given by a sum of Hamiltonians for each molecule, i.e.,  $H_s = \sum_{n \in \text{sample}} H_n$ . Moreover,  $\vec{\mathcal{V}}(\mathbf{r}) = \sum_{n \in \text{sample}} \vec{\mathcal{V}}_n \delta(\mathbf{r} - \mathbf{r}_n)$  is the macroscopic dipole de-excitation operator for the sample, which is written as the sum of de-excitation operators for each molecule in the sample. We assume that the de-excitation operators of the molecules correspond to electronic transitions in the ultraviolet regime. Finally, the sample–field interaction is written in the rotating-wave approximation. The electric field envelope of each pulse at the sample is approximated by a plane wave with its own central wave vector.

The proposed coincidence detection signal collects the outgoing fields from the sample in the directions  $\mathbf{k}_3$  and  $\mathbf{k}_4$  and mixes them with the reference pulses  $\tilde{3}$  and  $\tilde{4}$  (local oscillators) at the two beam splitters, respectively. This coincidence signal can be expressed in terms of the fields entering the 50 : 50 beam splitters, i.e., using Eq. (4) in Eq. (1),

Each term in the square brackets in Eq. (10) can be thought of as operators corresponding to a heterodyne detection, i.e., pulses  $\tilde{3}$  and  $\tilde{4}$ , individually heterodynes pulses 3 and 4. Since the signal measures the correlation/coincidence between the two heterodyne detections, we refer to our signal as the coincidence-double-heterodyne detection signal, indicated by the subscript  $\mathcal{DH}$ .

Since pulses,  $\tilde{3}$  and  $\tilde{4}$ , do not pass through the sample, the four-point field correlation function between the outgoing and the reference local oscillator fields can be decoupled. For the initial coherent states of the local oscillators, Eq. (5), the electric field operators can be replaced by classical electric field amplitudes to get

optical nonlinearity, acts as a medium for entangled photon pair generation [39–44]. We note that the diagrams corresponding to the double quantum coherence signal contribute only to the first term. In contrast, those corresponding to the non-rephasing and the photon-echo signals contribute only to the second term (see Supplement 1).

### 3. PATHWAY SELECTIVITY IN QUANTUM ULTRAFast PHOTON-ECHO SPECTROSCOPY

The four-wave mixing signals (see Supplement 1) are computed by expanding the coincidence signal defined in Eq. (11) to the fourth order in the system–field interaction. This gives

$$\mathcal{S}_{\mathcal{DH}} = 2 \left[ \prod_{i=3,4} \frac{1}{2\pi c_i c_i} \right] \frac{1}{4! \hbar^4} \text{Re} \int_{-\infty}^{+\infty} \cdots \int_{-\infty}^{+\infty} dt_4 dt_3 dt_2 \cdots dt_1 \left[ \langle \mathcal{T} \vec{E}_4^*(t_4) \cdot \vec{E}_{4L}(t_4) \vec{E}_3^*(t_3) \cdot \vec{E}_{3L}(t_3) \prod_{n=1}^4 H_{sf-}(t_n) \rangle_0 - \langle \mathcal{T} \vec{E}_4^*(t_4) \cdot \vec{E}_{4L}(t_4) \vec{E}_{3R}^\dagger(t_3) \cdot \vec{E}_3(t_3) \prod_{n=1}^4 H_{sf-}(t_n) \rangle_0 \right]. \quad (12)$$

Here  $\langle \cdots \rangle_0$  stands for expectation value with respect to the uncorrelated initial system and field state  $[\rho(-\infty)]$ . In the above equation, upon expanding each of  $H_{sf-}(t)$ , we find a total of  $2^9$  terms and their complex conjugates. As in conventional four-wave mixing spectroscopies, we only retain terms arising from a first-order interaction with each pulse. Below, we focus on the photon-echo signal; the other signals are discussed in Supplement 1. For homogeneous and isotropic samples, the physical macroscopic signal is obtained by translational and rotational averaging over all possible positions and orientations of  $N$  molecules that interact with the four pulses 1, 2, 3, 4. Thus, obtained macroscopic signal in the photon-echo phase-matching direction is given as

$$\begin{aligned} \mathcal{S}_{\mathcal{DH}}^{\text{PE}} &= -\frac{2(2\pi)^3}{\hbar^4} N \delta^{(3)}(\mathbf{k}_4 - \mathbf{k}_3 - \mathbf{k}_2 + \mathbf{k}_1) \\ &\text{Re} \int_{-\infty}^{+\infty} dt_4 \cdots \int_{-\infty}^{+\infty} dt_1 \sum_{n_4, \dots, n_1 = x, y, z} \\ &\left[ \langle \mathcal{V}_L^{n_4}(t_4) \mathcal{V}_R^{n_3^\dagger}(t_3) \mathcal{V}_L^{n_2^\dagger}(t_2) \mathcal{V}_R^{n_1}(t_1) \rangle_s \right. \\ &\quad \left. - \langle \mathcal{V}_L^{n_4}(t_4) \mathcal{V}_L^{n_2^\dagger}(t_2) \rangle_s \langle \mathcal{V}_R^{n_3^\dagger}(t_3) \mathcal{V}_R^{n_1}(t_1) \rangle_s \right] \\ &\times \mathcal{R}_{n_4, n_3, n_2, n_1}^T \begin{bmatrix} \vec{E}_3^*(t_4) \cdot \vec{E}_3(t_3) \vec{E}_2(t_2) \cdot \vec{E}_1^*(t_1) \\ \vec{E}_3^*(t_4) \cdot \vec{E}_2(t_2) \vec{E}_3(t_3) \cdot \vec{E}_1^*(t_1) \\ \vec{E}_4^*(t_4) \cdot \vec{E}_1^*(t_1) \vec{E}_3(t_3) \cdot \vec{E}_2(t_2) \end{bmatrix} \\ &- \frac{2(2\pi)^6}{\hbar^4} N^2 \delta^{(3)}(\mathbf{k}_4 - \mathbf{k}_2) \delta^{(3)}(\mathbf{k}_3 - \mathbf{k}_1) \\ &\text{Re} \int_{-\infty}^{+\infty} dt_4 \cdots \int_{-\infty}^{+\infty} dt_1 \\ &\frac{\langle \vec{\mathcal{V}}_L(t_4) \cdot \vec{\mathcal{V}}_L^\dagger(t_2) \rangle_s \langle \vec{\mathcal{V}}_R^\dagger(t_3) \cdot \vec{\mathcal{V}}_R(t_1) \rangle_s \times}{9} \\ &\frac{\vec{E}_4^*(t_4) \cdot \vec{E}_2(t_2) \vec{E}_3(t_3) \cdot \vec{E}_1^*(t_1)}{9}. \end{aligned} \quad (13)$$

Here

$$\mathcal{R}_{n_4, n_3, n_2, n_1} = \frac{1}{30} \begin{bmatrix} 4\delta_{n_4 n_3} \delta_{n_2 n_1} - \delta_{n_4 n_2} \delta_{n_3 n_1} - \delta_{n_4 n_1} \delta_{n_3 n_2} \\ -\delta_{n_4 n_3} \delta_{n_2 n_1} + 4\delta_{n_4 n_2} \delta_{n_3 n_1} - \delta_{n_4 n_1} \delta_{n_3 n_2} \\ -\delta_{n_4 n_3} \delta_{n_2 n_1} - \delta_{n_4 n_2} \delta_{n_3 n_1} + 4\delta_{n_4 n_1} \delta_{n_3 n_2} \end{bmatrix}.$$

See Supplement 1 for a detailed derivation of the signals in all phase-matching directions. In the above, we assumed that the classical pulse envelopes are temporally well separated and arrive at the sample in the sequence 1, 2, 3, 4.

The above signal has two distinct types of contributions [31,45–47], a single molecule contribution, which scales as  $N$  with the number of molecules, and a two-molecule contribution, which scales as  $N^2$ . The former contribution, which we refer to as genuine nonlinear response in the phase-matched direction  $\mathbf{k}_4 - \mathbf{k}_3 = \mathbf{k}_2 - \mathbf{k}_1$ , has two terms, the genuine single molecule contribution [Fig. 2(a)], and a pseudo two-molecule contribution [Fig. 2(b)], is given by the product of linear responses of two copies of the same molecule. Both of these terms scale as  $N$ . The latter contribution, which we refer to as the signal in the background phase-matched direction,  $\mathbf{k}_4 = \mathbf{k}_2$  and  $\mathbf{k}_3 = \mathbf{k}_1$ , is also given by the product of linear responses (absorption spectra) of two molecules. This is also represented by Fig. 2(b). Its contribution, in contrast, scales as  $N^2$ . We emphasize that, as a consequence of translational averaging detailed in Supplement 1, the disconnected diagram [Fig. 2(b)], contributes to the signal in both the background phase-matching direction, where its contribution scales as  $N^2$ , as well as to the signal in genuine photon-echo phase matching direction, where its contribution scales as  $N$ , hence may be thought of as pseudo-two-molecule contribution. We note that this disconnected diagram carries no additional information beyond linear absorption spectroscopy. However, these unwanted  $N^2$  contributions can be suppressed (i) by collecting the signals in directions  $\mathbf{k}_{3/4}$  distinct from the propagation directions of the incoming pulses,  $\mathbf{k}_{1/2}$ , or (ii) by using linearly polarized pulses and collecting pulses 3 and 4 with polarization vectors,  $\epsilon_{3/4}$ , orthogonal to those of 1 and 2,  $\epsilon_{1/2}$ . Despite eliminating this background, the disconnected diagram contribution, which scales as  $N$ , the pseudo-two-molecule contribution, still contributes to the signal in the genuine photon-echo phase-matching direction. This pseudo-two-molecule contribution, a consequence of translational averaging, cannot be eliminated from the signal. However, as discussed later, its contribution is expected to rapidly decay as a function of the time delay between the second and third pulses. By collecting signals in the photon-echo phase matching direction  $\mathbf{k}_4 - \mathbf{k}_3 = \mathbf{k}_2 - \mathbf{k}_1$  (with the additional constraint of  $\mathbf{k}_4 \neq \mathbf{k}_2$  and  $\mathbf{k}_3 \neq \mathbf{k}_1$ ), we obtain the following expression for the signal:

$$\begin{aligned} \mathcal{S}_{\mathcal{DH}}^{\text{PE}} &= -\frac{2}{\hbar^4} \text{Re} \int_{-\infty}^{+\infty} dt_4 \cdots \int_{-\infty}^{+\infty} dt_1 \sum_{n_4, \dots, n_1 = x, y, z} \\ &\left[ \langle \mathcal{V}_L^{n_4}(t_4) \mathcal{V}_R^{n_3^\dagger}(t_3) \mathcal{V}_L^{n_2^\dagger}(t_2) \mathcal{V}_R^{n_1}(t_1) \rangle_s \right. \\ &\quad \left. - \langle \mathcal{V}_L^{n_4}(t_4) \mathcal{V}_L^{n_2^\dagger}(t_2) \rangle_s \langle \mathcal{V}_R^{n_3^\dagger}(t_3) \mathcal{V}_R^{n_1}(t_1) \rangle_s \right] \\ &\times \mathcal{R}_{n_4, n_3, n_2, n_1}^T \begin{bmatrix} \vec{E}_3^*(t_4) \cdot \vec{E}_3(t_3) \vec{E}_2(t_2) \cdot \vec{E}_1^*(t_1) \\ \vec{E}_3^*(t_4) \cdot \vec{E}_2(t_2) \vec{E}_3(t_3) \cdot \vec{E}_1^*(t_1) \\ \vec{E}_4^*(t_4) \cdot \vec{E}_1^*(t_1) \vec{E}_3(t_3) \cdot \vec{E}_2(t_2) \end{bmatrix}. \end{aligned} \quad (14)$$

Here, we have dropped inconsequential factor of  $(2\pi)^3 N \delta^{(3)}(\mathbf{k}_4 - \mathbf{k}_3 - \mathbf{k}_2 + \mathbf{k}_1)$ . The above signal then probes the difference of the ladder diagrams in Fig. 2, i.e., the diagram in Fig. 2(a) and its corresponding disconnected diagram Fig. 2(b). We note that in macroscopic samples, it is not possible to fully isolate diagram Fig. 2(a). Although the diagrams in Figs. 1(b) and 1(c) and their corresponding disconnected contributions satisfy the same phase matching condition as Fig. 1(a) and its corresponding disconnected contribution, they do not contribute to  $\mathcal{S}_{\mathcal{DH}}^{\text{PE}}$ . This is because the diagrams in Figs. 1(b) and 1(c) involve the

absorption of a photon from pulse 3 which is initially in the vacuum state. However, if the time ordering of pulses 2 and  $\bar{3}$  is interchanged in Fig. 3, the coincidence signal can selectively isolate the diagram in Fig. 1(c) along with its disconnected contribution. Hereafter, we refer to the above signal as the quantum signal.

We next contrast the quantum signal,  $\mathcal{S}_{\mathcal{D}\mathcal{H}}^{\text{PE}}$ , with the standard classical heterodyne detected photon-echo signal, where a single pulse, 4, is detected. For temporally well-separated pulses,  $\{\vec{E}_1(t), \dots, \vec{E}_4(t)\}$  this signal is given by

$$\begin{aligned} \mathcal{S}_{\mathcal{H}}^{\text{PE}} = & -\frac{2}{\hbar^4} \text{Re} \int_{-\infty}^{+\infty} dt_4 \cdots \int_{-\infty}^{+\infty} dt_1 \sum_{n_4, \dots, n_1 = x, y, z} \\ & \left[ \langle \mathcal{V}_L^{n_4}(t_4) \mathcal{V}_R^{n_3^\dagger}(t_3) \mathcal{V}_L^{n_2^\dagger}(t_2) \mathcal{V}_R^{n_1}(t_1) \rangle_s \right. \\ & - \langle \mathcal{V}_L^{n_4}(t_4) \mathcal{V}_L^{n_3^\dagger}(t_3) \mathcal{V}_L^{n_2^\dagger}(t_2) \mathcal{V}_R^{n_1}(t_1) \rangle_s \\ & \left. + \langle \mathcal{V}_L^{n_4}(t_4) \mathcal{V}_L^{n_3^\dagger}(t_3) \mathcal{V}_R^{n_2^\dagger}(t_2) \mathcal{V}_R^{n_1}(t_1) \rangle_s \right] \\ & \times \mathcal{R}_{n_4, n_3, n_2, n_1}^T \begin{bmatrix} \vec{E}_3^*(t_4) \cdot \vec{E}_5(t_3) \vec{E}_2(t_2) \cdot \vec{E}_1^*(t_1) \\ \vec{E}_3^*(t_4) \cdot \vec{E}_2(t_2) \vec{E}_3(t_3) \cdot \vec{E}_1^*(t_1) \\ \vec{E}_4^*(t_4) \cdot \vec{E}_1(t_1) \vec{E}_3(t_3) \cdot \vec{E}_2(t_2) \end{bmatrix}. \end{aligned} \quad (15)$$

Hereafter, we refer to this signal as the classical signal.

This signal has contributions given by the sum of all diagrams in Fig. 1. The sum of contributions from the disconnected diagrams corresponding to Fig. 1 vanishes.

We note that the sum of all diagrams contributing to the classical signal,  $\mathcal{S}_{\mathcal{H}}^{\text{PE}}$ , can be expressed in terms of the classical causal response function  $\chi_{+---}^{(3)}(n_1, \dots, n_4; t_1, \dots, t_4) = \langle \mathcal{V}_+^{n_4}(t_4) \mathcal{V}_-^{n_3^\dagger}(t_3) \mathcal{V}_-^{n_2^\dagger}(t_2) \mathcal{V}_-^{n_1}(t_1) \rangle_s$ . The quantum signal,  $\mathcal{S}_{\mathcal{D}\mathcal{H}}^{\text{PE}}$  cannot be expressed solely in terms of such causal response functions. Although it can be expressed as a combination of causal and non-causal response functions,  $\chi_{+---}^{(3)}(n_1, \dots, n_4; t_1, \dots, t_4)$ . The same conclusions hold for the signals in other phase-matching directions discussed in Supplement 1. Therefore, measuring several outgoing fields, as is done in the present coincidence scheme, provides a rich avenue to access non-causal response functions of material systems [26,32,48].

Since the double-heterodyne detection scheme in the photon-echo phase-matching direction selects Fig. 1(a) [along with its disconnected piece, Fig. 2(b)] from the contributions to the classical signal, we call this pathway selectivity. Hence, measuring more than a single pulse provides pathway selectivity in our quantum signal. The proposed detection scheme also achieves pathway selectivity for the signals in phase-matching directions other than the photon echo; this is discussed in Supplement 1.

#### 4. CLASSICAL VERSUS QUANTUM ULTRAFAST PHOTON-ECHO SIGNALS IN THE IMPULSIVE LIMIT

We now consider the impulsive limit with linearly polarized pulses, where classical electric fields are given by

$$\vec{E}_n(t) = \epsilon_n \sqrt{I} e^{-i\omega t} \delta(t - \tau_n) \quad n = 1, \dots, 4,$$

with the conditions  $\tau_4 > \dots > \tau_1$  and  $\epsilon_4^* \cdot \epsilon_2 = \epsilon_4^* \cdot \epsilon_1 = \epsilon_3^* \cdot \epsilon_2 = \epsilon_3^* \cdot \epsilon_1 = 0$ , and  $\epsilon_4^* \cdot \epsilon_3 = \epsilon_2^* \cdot \epsilon_1 = 1$ . Here,  $I$  is the intensity of

pulses 1, 2,  $\bar{3}$ ,  $\bar{4}$ . For this pulse configuration, the quantum and classical photon-echo signals are simplified to

$$\begin{aligned} \mathcal{S}_{\mathcal{D}\mathcal{H}}^{\text{PE}}(\tau_1, \dots, \tau_4) = & -\frac{I^2}{15\hbar^4} \sum_{n_4, \dots, n_1 = x, y, z} \\ & (4\delta_{n_4 n_3} \delta_{n_2 n_1} - \delta_{n_4 n_2} \delta_{n_3 n_1} - \delta_{n_3 n_2} \delta_{n_4 n_1}) \times \\ & \left[ \langle \mathcal{V}_L^{n_4}(\tau_4) \mathcal{V}_R^{n_3^\dagger}(\tau_3) \mathcal{V}_L^{n_2^\dagger}(\tau_2) \mathcal{V}_R^{n_1}(\tau_1) \rangle_s \right. \\ & \left. - \langle \mathcal{V}_L^{n_4}(\tau_4) \mathcal{V}_L^{n_2^\dagger}(\tau_2) \rangle_s \langle \mathcal{V}_R^{n_3^\dagger}(\tau_3) \mathcal{V}_R^{n_1}(\tau_1) \rangle_s \right] \end{aligned} \quad (16)$$

and

$$\begin{aligned} \mathcal{S}_{\mathcal{H}}^{\text{PE}}(\tau_1, \dots, \tau_4) = & -\frac{I^2}{15\hbar^4} \sum_{n_4, \dots, n_1 = x, y, z} \\ & (4\delta_{n_4 n_3} \delta_{n_2 n_1} - \delta_{n_4 n_2} \delta_{n_3 n_1} - \delta_{n_3 n_2} \delta_{n_4 n_1}) \times \\ & \left[ \langle \mathcal{V}_L^{n_4}(\tau_4) \mathcal{V}_R^{n_3^\dagger}(\tau_3) \mathcal{V}_L^{n_2^\dagger}(\tau_2) \mathcal{V}_R^{n_1}(\tau_1) \rangle_s \right. \\ & - \langle \mathcal{V}_L^{n_4}(\tau_4) \mathcal{V}_L^{n_3^\dagger}(\tau_3) \mathcal{V}_L^{n_2^\dagger}(\tau_2) \mathcal{V}_R^{n_1}(\tau_1) \rangle_s \\ & \left. + \langle \mathcal{V}_L^{n_4}(\tau_4) \mathcal{V}_L^{n_3^\dagger}(\tau_3) \mathcal{V}_R^{n_2^\dagger}(\tau_2) \mathcal{V}_R^{n_1}(\tau_1) \rangle_s \right]. \end{aligned} \quad (17)$$

For molecules initially in a stationary state, e.g., the ground state  $|g\rangle\langle g|$ , the signals in Eqs. (17) and (16) are independent of  $\tau_1$ . It is then convenient to express the above signals in terms of the time delays between consecutive pulses,  $T_n = \tau_{n+1} - \tau_n$  ( $n = 1, 2, 3$ ). Furthermore, as is customary in the four-wave mixing spectroscopies [1,7,49], these signals are conveniently expressed as half-Fourier-transforms with respect to  $T_1$  and  $T_3$  as

$$\begin{aligned} \mathcal{S}_{\mathcal{H}/\mathcal{D}\mathcal{H}}^{\text{PE}}(\Omega_1, T_2, \Omega_3) \\ = \int_0^\infty dT_3 \int_0^\infty dT_1 e^{i\Omega_3 T_3 + i\Omega_1 T_1} \mathcal{S}_{\mathcal{H}/\mathcal{D}\mathcal{H}}^{\text{PE}}(T_1, T_2, T_3). \end{aligned} \quad (18)$$

Sum-over-states expressions can provide insight into the information revealed by each of the signals,  $\mathcal{S}_{\mathcal{H}/\mathcal{D}\mathcal{H}}^{\text{PE}}$ . These expressions, for a generic molecular aggregate with energy levels grouped into (i) ground ( $|g\rangle$ ), (ii) single exciton ( $\{|e_1\rangle, \dots, |e_N\rangle\}$ ), and (iii) two exciton ( $\{|f_1\rangle, \dots, |f_M\rangle\}$ ) manifolds [see Fig. 4(b)], coupled to a Markovian bath, are given

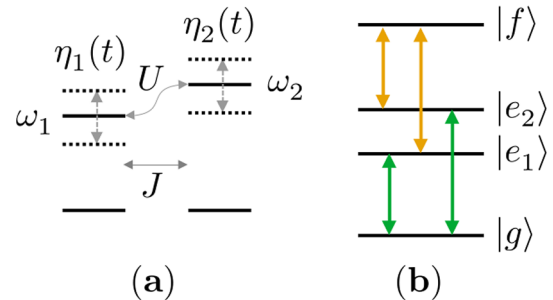


**Fig. 4.** The model system used for the computation of signals presented in Fig. 5. (a) The Frenkel dimer model consisting of two two-level molecules that are coupled through both the static and the transition dipoles of each molecule. Site energies undergo stochastic fluctuations. (b) In the absence of the noise, the model's eigenstates are grouped into the ground manifold ( $|g\rangle$ ), single exciton manifold ( $\{|e_1\rangle, |e_2\rangle\}$ ), and two exciton manifold ( $|f\rangle$ ). Please see Table 1, for the nature of parameters used for simulations.

as

$$\begin{aligned} \mathcal{S}_{\mathcal{DH}}^{\text{PE}}(\Omega_1, T_2, \Omega_3) &= \mathcal{S}_{\mathcal{DH}}^{\text{PE,SE}}(\Omega_1, T_2, \Omega_3) \\ &\quad - \mathcal{S}_{\mathcal{DH}}^{\text{PE,SE,DC}}(\Omega_1, T_2, \Omega_3) \end{aligned} \quad (19)$$

and

$$\begin{aligned} \mathcal{S}_{\mathcal{H}}^{\text{PE,SE}}(\Omega_1, T_2, \Omega_3) &= \sum_{n_4, \dots, n_1=x,y,z} (4\delta_{n_4 n_3} \delta_{n_2 n_1} - \delta_{n_4 n_2} \delta_{n_3 n_1} - \delta_{n_3 n_2} \delta_{n_4 n_1}) \sum_{e, e', \bar{e}, \bar{e}'} \frac{\mu_{g\bar{e}}^{n_4} \mu_{e'g}^{n_3} \mu_{e\bar{e}}^{n_2} \mu_{g\bar{e}'}^{n_1} \mathcal{G}_{\bar{e}, \bar{e}'; e, e'}(T_2)}{(\Omega_3 - \omega_{\bar{e}g} + i\gamma_{\bar{e}g}) (-\Omega_1 - \omega_{e'g} - i\gamma_{e'g})} \\ \mathcal{S}_{\mathcal{DH}}^{\text{PE,SE,DC}}(\Omega_1, T_2, \Omega_3) &= \sum_{n_4, \dots, n_1=x,y,z} (4\delta_{n_4 n_3} \delta_{n_2 n_1} - \delta_{n_4 n_2} \delta_{n_3 n_1} - \delta_{n_3 n_2} \delta_{n_4 n_1}) \sum_{\bar{e}, e'} \frac{\mu_{g\bar{e}}^{n_4} \mu_{e'g}^{n_3} \mu_{e\bar{e}}^{n_2} \mu_{g\bar{e}'}^{n_1} e^{-i(\omega_{e'} - i\gamma_{e'} - i\gamma_{e'g})T_2}}{(\Omega_3 - \omega_{\bar{e}g} + i\gamma_{\bar{e}g}) (-\Omega_1 - \omega_{e'g} - i\gamma_{e'g})} \\ \mathcal{S}_{\mathcal{DH}}^{\text{PE,SE}}(\Omega_1, T_2, \Omega_3) &= \mathcal{S}_{\mathcal{H}}^{\text{PE,SE}}(\Omega_1, T_2, \Omega_3) \\ \mathcal{S}_{\mathcal{H}}^{\text{PE,ESA}}(\Omega_1, T_2, \Omega_3) &= \sum_{n_4, \dots, n_1=x,y,z} (4\delta_{n_4 n_3} \delta_{n_2 n_1} - \delta_{n_4 n_2} \delta_{n_3 n_1} - \delta_{n_3 n_2} \delta_{n_4 n_1}) \sum_{e, e', \bar{e}, \bar{e}'} \frac{-\mu_{e'f}^{n_4} \mu_{f\bar{e}}^{n_3} \mu_{e\bar{e}}^{n_2} \mu_{g\bar{e}'}^{n_1} \mathcal{G}_{\bar{e}, \bar{e}'; e, e'}(T_2)}{(\Omega_3 - \omega_{f\bar{e}} + i\gamma_{f\bar{e}}) (-\Omega_1 - \omega_{e'g} - i\gamma_{e'g})} \\ \mathcal{S}_{\mathcal{H}}^{\text{PE,GSB}}(\Omega_1, T_2, \Omega_3) &= \sum_{n_4, \dots, n_1=x,y,z} (4\delta_{n_4 n_3} \delta_{n_2 n_1} - \delta_{n_4 n_2} \delta_{n_3 n_1} - \delta_{n_3 n_2} \delta_{n_4 n_1}) \sum_{\bar{e}, e'} \frac{\mu_{g\bar{e}}^{n_4} \mu_{e'g}^{n_3} \mu_{e\bar{e}}^{n_2} \mu_{g\bar{e}'}^{n_1}}{(\Omega_3 - \omega_{\bar{e}g} + i\gamma_{\bar{e}g}) (-\Omega_1 - \omega_{e'g} - i\gamma_{e'g})}, \end{aligned} \quad (24)$$

where  $\mu_{xy}^n = \langle x | \mu^n | y \rangle$  is the transition de-excitation operator and  $\gamma_{xy}$  is the dephasing rate between states  $x$  and  $y$ . Here  $\mathcal{G}_{\bar{e}, \bar{e}'; e, e'}(t) = \langle \langle |\bar{e}\rangle \langle \bar{e}' | e^{\mathcal{L}t} | e\rangle \langle e' | \rangle \rangle$  are the matrix elements of the Liouville space propagation superoperator in the single exciton manifold, which in the secular approximation (Lindblad evolution) which decouples populations and coherences in the exciton eigenbasis [7,50], are given by  $\mathcal{G}_{\bar{e}, \bar{e}'; e, e'}(t) = \delta_{\bar{e}\bar{e}'} \delta_{e'e} e^{-i(\omega_{e'} - i\gamma_{e'} - i\gamma_{e'g})t} + \delta_{\bar{e}\bar{e}'} \delta_{e'e} \langle \bar{e} | e^{\mathcal{W}t} | e \rangle$ , where  $\mathcal{W}$  is the population relaxation matrix.

When exciton relaxation is neglected or treated phenomenologically, i.e., either (i) for isolated aggregates without dissipation, or (ii) for treatments of relaxation dynamics through the addition of negative imaginary relaxation rates to exciton energy states,  $\mathcal{S}_{\mathcal{DH}}^{\text{PE,SE}} = \mathcal{S}_{\mathcal{DH}}^{\text{PE,SE,DC}}$  and hence the quantum signal,  $\mathcal{S}_{\mathcal{DH}}^{\text{PE}}$ , vanishes. Therefore, the quantum signal is sensitive to the relaxation dynamics of molecular aggregates.

In the sum-over-states representation [Eqs. (19)],  $\Omega_1$  covers the energy gap between the single and zero exciton manifolds;  $T_2$  covers the temporal dynamics of population and coherences in the single exciton manifold [Figs. 1(a) and 1(b)] and in the zero exciton manifold [Fig. 1(c)];  $\Omega_3$  provides information of the energy gap between the single and zero exciton manifolds [Figs. 1(a) and 1(c)] and the two exciton and single exciton manifolds [Fig. 1(b)]. Two types of resonances appear in  $\mathcal{S}_{\mathcal{H}(\mathcal{DH})}^{\text{PE}}$ : (i) diagonal ( $\Omega_1 = -\Omega_3$ ), and (ii) off-diagonal ( $\Omega_1 \neq -\Omega_3$ ). For both diagonal and off-diagonal resonances, in  $\mathcal{S}_{\mathcal{H}}^{\text{PE}}$ , generically all diagrams in Fig. 1 contribute. Hence their interference can complicate the interpretation of the signal. Only one diagram [after  $T_2$  greater than the decoherence time of single and zero exciton manifolds, Fig. 2(a)] contributes to  $\mathcal{S}_{\mathcal{DH}}^{\text{PE}}$ . When only the dynamics in the single exciton manifold is of interest, it can be advantageous to study  $\mathcal{S}_{\mathcal{DH}}^{\text{PE}}$ , as its computation and measurement do not involve any knowledge of the two-exciton manifold. Hence, the proposed quantum signal should be useful for probing exciton dynamics in molecular and biological aggregates [7,49,51,52], where the experimentally obtained dynamical time scales are predominantly rationalized based on phenomenological models. The proposed technique requires fewer parameters to reconstruct the experimental signal.

## 5. APPLICATION TO A FRENKEL-EXCITON DIMER

We now compare the quantum and the classical photon-echo signals for a Frenkel dimer model [7,51–53]. As sketched in Fig. 4(a), this model consists of two coupled two-level Frenkel sites [described by two-level system de-excitation operators  $\{B_1, B_2\}$ , which satisfy the commutation relations  $[B_m, B_n^\dagger] = \delta_{mn}(1 - 2B_n^\dagger B_n)$ ]. The local dephasing of the Frenkel sites is modeled by stochastic fluctuations of their site energies. This system is described by the Hamiltonian

$$H(t) = \sum_{m,n=1}^2 h_{mn}(t) B_m^\dagger B_n + U B_1^\dagger B_1 B_2^\dagger B_2, \quad (25)$$

where the single exciton Hamiltonian is given by  $h(t) = \begin{pmatrix} \omega_1 + \eta_1(t) & J \\ J & \omega_2 + \eta_2(t) \end{pmatrix}$ . Here, the classical stochastic process  $\eta_n(t)$  represents an uncorrelated Gaussian colored noise statistics with zero mean and variance  $\langle \eta_n(t) \eta_{n'}(t') \rangle = \delta_{nn'} \alpha_n^2 e^{-\gamma_n |t-t'|}$ . The de-excitation component of the transition dipole operator is given by  $\vec{\mathcal{V}} = \sum_{n=1}^2 \vec{\mu}_n B_n$ . The parameters used in the simulations, along with their physical interpretation, are given in Table 1.

In the absence of noise, the eigenstates of  $H$  are (i) the ground state  $|g\rangle$  (such that  $B_n |g\rangle = 0$ ) with energy  $\omega_g = 0$ ; (ii) the single

**Table 1. Parameters for the Frenkel Dimer Used for Simulations<sup>a</sup>**

$\omega_1$	$\omega_2$	$J$	$U$	$\alpha_1 = \alpha_2$	$\gamma_1 = \gamma_2$	$\vec{\mu}_1$	$\vec{\mu}_2$
1.95 eV	2.05 eV	0.1 eV	0.05 eV	0.05 eV	0.02 eV	$1\hat{x} \text{ D}$	$1\hat{y} \text{ D}$

<sup>a</sup>Here,  $\omega_1$  and  $\omega_2$  represent the transition energy gaps of isolated Frenkel sites;  $J$  represents the transition dipole coupling between the Frenkel sites;  $U$  represents the static dipole coupling between Frenkel sites. It can also be interpreted as exciton-exciton binding/repulsion energy. Here  $\alpha_1, \alpha_2, \gamma_1$ , and  $\gamma_2$  characterize the Gaussian colored noise used to model dephasing and transport in the Frenkel model;  $\vec{\mu}_1$  and  $\vec{\mu}_2$  correspond to transition dipole vectors for each isolated Frenkel sites.

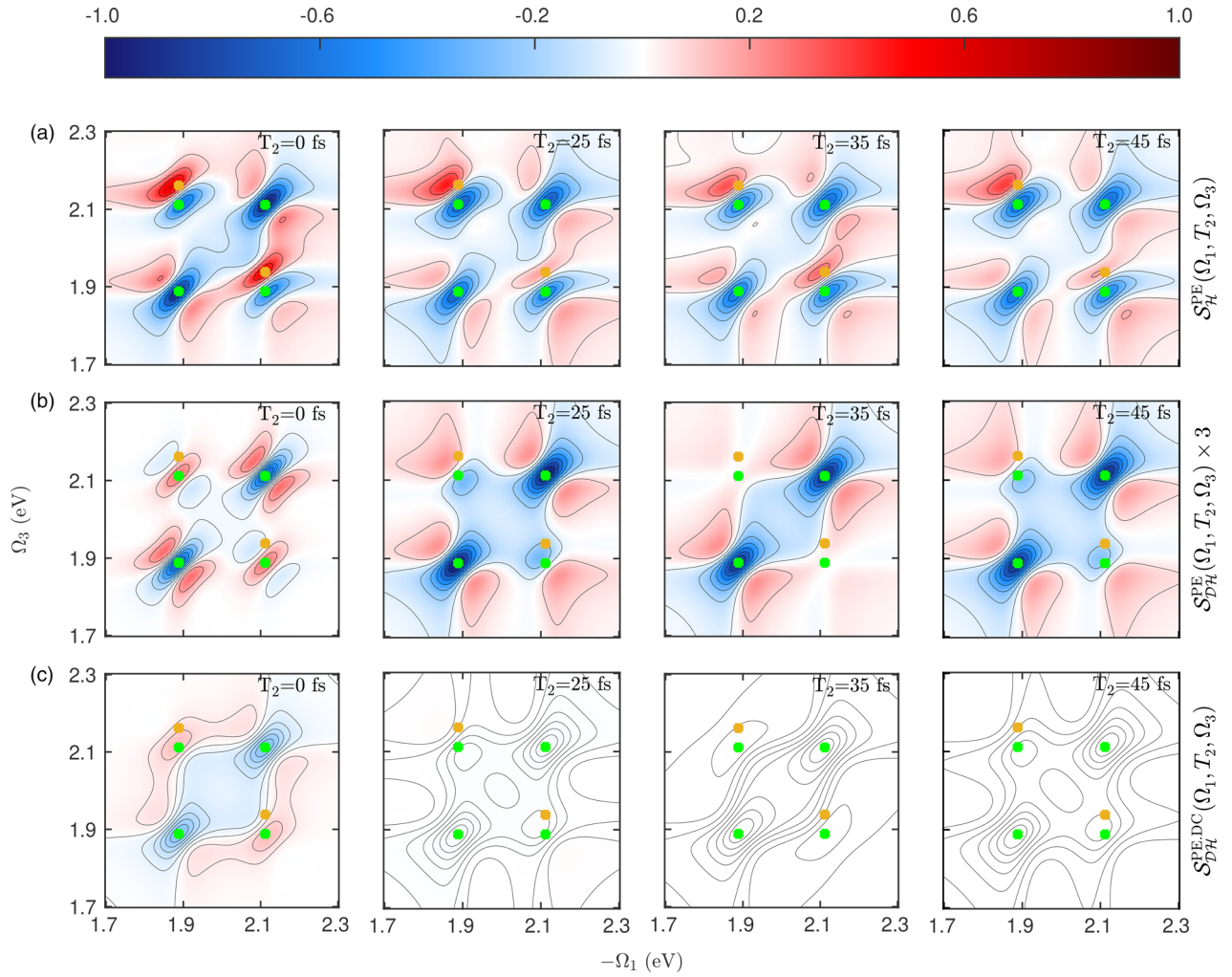


**Fig. 5.** Here (a)  $S_{\mathcal{H}}^{\text{PE}}$  (sum of all diagrams in Fig. 1), (b)  $S_{\mathcal{DH}}^{\text{PE}}$  (difference of the diagrams in Fig. 2), and (c) disconnected contribution to  $S_{\mathcal{DH}}^{\text{PE}}$  [diagram in Fig. 2(b)] for various waiting times ( $T_2$ ). Green and yellow markers indicate the location of resonances from various Liouville space pathways. Green represents resonances that appear in the diagrams in Figs. 1(a) and 1(c), and yellow represents those in Fig. 1(b).

exciton states,  $|e_{1/2}\rangle = [\cos\theta B_1^\dagger \mp \sin\theta B_2^\dagger]|g\rangle$  ( $\theta$  is the mixing angle determined such that the rotational matrix  $R(\theta) = e^{i\theta\sigma_y}$  diagonalizes the single-exciton Hamiltonian  $h(t)|_{\eta_n(t)=0}$  with their respective energies  $\omega_{e_{1/2}}$ ; and (iii) the two exciton state  $|f\rangle = B_1^\dagger B_2^\dagger|g\rangle$  with the energy  $\omega_f = \omega_1 + \omega_2 + U$ .

We have computed the signals  $S_{\mathcal{H}/\mathcal{DH}}^{\text{PE}}$  using the hierarchical equations of motion method [54–58]. Computed signals are plotted in Fig. 5 and Visualization 1. See Supplement 1 for technical and computational details.

As discussed below, the quantum and classical signals plotted in Fig. 5 and Visualization 1 show distinct features. Two key differences are (i) off-diagonal resonances appearing from the excited state absorption diagram [Fig. 1(b)] in the classical signal are absent in the quantum signal, and (ii) after a short transient time, ground state bleach contribution [Fig. 1(c)] to both the diagonal and off-diagonal resonances in the classical signal is absent in the quantum signal. These differences reduce spectral

congestion and background in the quantum signal, making it easier to interpret.

Figure 5(a) corresponds to the classical photon-echo signal,  $S_{\mathcal{H}}^{\text{PE}}$ , the sum of all diagrams in Fig. 1. Figure 5(b) is the quantum signal,  $S_{\mathcal{DH}}^{\text{PE}}$ , the difference of the diagrams in Fig. 2. Figure 5(c) is the disconnected contribution to  $S_{\mathcal{DH}}^{\text{PE}}$ , the diagram in Fig. 2(b). The dynamics probed during  $T_2$  by the disconnected contribution [Fig. 2(b)] to  $S_{\mathcal{DH}}^{\text{PE}}$  is dictated by the dephasing between the single and zero exciton manifolds. As the dephasing times between the single and zero exciton manifolds are typically much faster than the time scales of dynamics in the single exciton manifold, this disconnected piece vanishes after a short transient time. For example, for the parameters chosen here, this disconnected contribution drops below 10% of the total signal,  $S_{\mathcal{DH}}^{\text{PE}}$ , for  $T_2 \geq 20$  fs. Therefore, the double-heterodyne detected signal,  $S_{\mathcal{DH}}^{\text{PE}}$ , effectively selects the single diagram in Fig. 2(a) after a short waiting time  $T_2$ .

The green and yellow markers in Fig. 5 indicate all possible resonances. Green markers represent the possible Liouville space pathways that contribute to the diagrams in Fig. 1(a) (the pathways  $|g\rangle\langle g| \xrightarrow{\tau_1} |g\rangle\langle e'| \xrightarrow{\tau_2} |e\rangle\langle e'| \rightsquigarrow |\bar{e}\rangle\langle \bar{e}'| \xrightarrow{\tau_3} |\bar{e}\rangle\langle g'| \rightarrow |g\rangle\langle g|$ ) and Fig. 1(c) (the pathways  $|g\rangle\langle g| \xrightarrow{\tau_1} |g\rangle\langle e'| \xrightarrow{\tau_2} |g\rangle\langle g| \xrightarrow{\tau_3} |\bar{e}\rangle\langle g'| \rightarrow |g\rangle\langle g|$ ). The diagonal green resonances ( $\Omega_3 = -\Omega_1$ ) probe these pathways with  $|e'\rangle = |\bar{e}\rangle$ , while the off-diagonal ones probe  $|e'\rangle \neq |\bar{e}\rangle$ . Yellow markers represent the Liouville space pathways that contribute to the diagram in Fig. 1(b) (the pathways  $|g\rangle\langle g| \xrightarrow{\tau_1} |g\rangle\langle e'| \xrightarrow{\tau_2} |e\rangle\langle e'| \rightsquigarrow |\bar{e}\rangle\langle \bar{e}'| \xrightarrow{\tau_3} |f\rangle\langle \bar{e}'| \rightarrow |\bar{e}'\rangle\langle \bar{e}'|$ ). Time dependence of the off-diagonal peaks give information on the dynamics in the single exciton manifold. Off-diagonal green resonances have contributions from both diagrams in Figs. 1(a) and 1(c). Moreover, for  $U \rightarrow 0$ , the yellow markers overlap with the off-diagonal green markers. This leads to the destructive interference of the contributions from Figs. 1(a) and 1(c) with that from Fig. 1(b). This complicates the interpretation of the signal. Such interfering pathways are avoided in the proposed quantum signal  $\mathcal{S}_{DH}^{PE}$ , which selects the diagrams in Figs. 2. This can simplify further analysis of single exciton dynamics. This can be seen from the absence of resonances at the yellow markers and the ground state bleach background at the off-diagonal green markers in the middle column of Fig. 5. In Visualization 1, both the signals,  $\mathcal{S}_{DH}^{PE}$  and  $\mathcal{S}_H^{PE}$ , are plotted for a series of time delays ( $T_2$ ). The absence of off-diagonal resonances from Fig. 1(b) and the background contribution to the off-diagonal resonances from Fig. 1(c), makes the coherent oscillations of the off-diagonal peaks in the signal  $\mathcal{S}_{DH}^{PE}$  easy to observe as opposed to the standard signal  $\mathcal{S}_H^{PE}$ . This absence of interfering contribution from the ground state bleaching, Fig. 1(c), to the signal  $\mathcal{S}_{DH}^{PE}$ , can be advantageous in two-dimensional electronic-vibrational spectroscopy [59,60]. Moreover, since the signal  $\mathcal{S}_{DH}^{PE}$  does not carry any information of the two exciton states, it can reduce the number of parameters needed to build the phenomenological models used for the interpretation of the experimental data on the single exciton dynamics. Hence, the proposed signal can probe dynamics in the single exciton manifold without the ground state bleach background and the knowledge of the two excitation manifold.

## 6. CONCLUSIONS

The proposed double-heterodyne coincidence detection scheme, which employs two classical and two vacuum fields, can single out a single pathway contributing to the signals measured in each of the three dominant phase matching directions in the four-wave mixing spectroscopies. This is illustrated for the photon-echo signal. Such selectivity has an advantage in interpreting the signals from molecules with complex vibronic and electronic dynamics in the condensed phase. This is demonstrated by computing the photon-echo signals obtained using the standard heterodyne and the proposed coincident double-heterodyne detection schemes for a Frenkel dimer model. The proposed coincident double-heterodyne signal should help understand the exciton dynamics in complex molecular aggregates.

**Funding.** Alexander von Humboldt-Stiftung (Feodor Lynen program);

Directorate for Mathematical and Physical Sciences (CHE-2246379); Basic Energy Sciences (DESC0022134).

**Acknowledgement.** S.M. gratefully acknowledges the support of the US Department of Energy, Office of Science, Basic Energy Sciences Award DESC0022134, which has primarily funded this work. H.K.Y. gratefully acknowledges the support of the National Science Foundation (grant CHE-2246379). M.K. acknowledges the support from the Alexander von Humboldt Foundation through the Feodor Lynen program. S.M. is a senior fellow at the Hagler Institute of Advanced Study at Texas AM. We thank Dr. Jérémy R. Rouxel for useful discussions.

**Disclosures.** The authors declare no conflicts of interest.

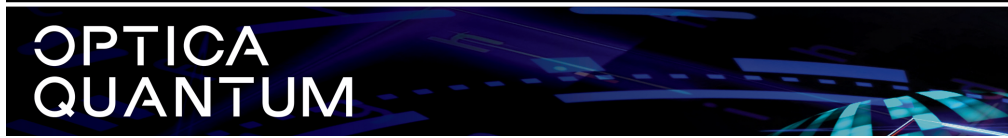
**Data availability.** Data underlying the results presented in this paper are not publicly available at this time but may be obtained from the authors upon reasonable request.

**Supplemental document.** See Supplement 1 for supporting content.

## REFERENCES

1. S. Mukamel, *Principles of Nonlinear Optical Spectroscopy* (Oxford University Press, 1995).
2. S. Mukamel, "Multidimensional femtosecond correlation spectroscopies of electronic and vibrational excitations," *Annu. Rev. Phys. Chem.* **51**, 691–729 (2000).
3. M. Cho, "Coherent two-dimensional optical spectroscopy," *Chem. Rev.* **108**, 1331–1418 (2008).
4. M. Cho, *Two-dimensional Optical Spectroscopy* (CRC press, 2009).
5. D. M. Jonas, "Two-dimensional femtosecond spectroscopy," *Annu. Rev. Phys. Chem.* **54**, 425–463 (2003).
6. S. Mukamel, D. Abramavicius, L. Yang, *et al.*, "Coherent multidimensional optical probes for electron correlations and exciton dynamics: From NMR to X-rays," *Acc. Chem. Res.* **42**, 553–562 (2009).
7. D. Abramavicius, B. Palmieri, D. V. Voronine, *et al.*, "Coherent multidimensional optical spectroscopy of excitons in molecular aggregates; quasiparticle versus supermolecule perspectives," *Chem. Rev.* **109**, 2350–2408 (2009).
8. K. E. Dorfman, F. Schlawin, and S. Mukamel, "Nonlinear optical signals and spectroscopy with quantum light," *Rev. Mod. Phys.* **88**, 045008 (2016).
9. S. Mukamel, M. Freyberger, W. Schleich, *et al.*, "Roadmap on quantum light spectroscopy," *J. Phys. B: At. Mol. Opt. Phys.* **53**, 072002 (2020).
10. S. Szoke, H. Liu, B. P. Hickam, *et al.*, "Entangled light-matter interactions and spectroscopy," *J. Mater. Chem. C* **8**, 10732–10741 (2020).
11. A. Eshun, O. Varnavski, J. P. Villabona-Monsalve, *et al.*, "Entangled photon spectroscopy," *Acc. Chem. Res.* **55**, 991–1003 (2022).
12. M. G. Raymer, T. Landes, and A. H. Marcus, "Entangled two-photon absorption by atoms and molecules: A quantum optics tutorial," *J. Chem. Phys.* **155**, 081501 (2021).
13. J. Gea-Banacloche, "Two-photon absorption of nonclassical light," *Phys. Rev. Lett.* **62**, 1603–1606 (1989).
14. J. Javanainen and P. L. Gould, "Linear intensity dependence of a two-photon transition rate," *Phys. Rev. A* **41**, 5088–5091 (1990).
15. N. P. Georgiades, E. S. Polzik, K. Edamatsu, *et al.*, "Nonclassical excitation for atoms in a squeezed vacuum," *Phys. Rev. Lett.* **75**, 3426–3429 (1995).
16. B. E. A. Saleh, B. M. Jost, H.-B. Fei, *et al.*, "Entangled-photon virtual-state spectroscopy," *Phys. Rev. Lett.* **80**, 3483–3486 (1998).
17. A. Muthukrishnan, G. S. Agarwal, and M. O. Scully, "Inducing disallowed two-atom transitions with temporally entangled photons," *Phys. Rev. Lett.* **93**, 093002 (2004).
18. A. Svidzinsky, G. Agarwal, A. Classen, *et al.*, "Enhancing stimulated Raman excitation and two-photon absorption using entangled states of light," *Phys. Rev. Res.* **3**, 043029 (2021).
19. Z. Zhang, T. Peng, X. Nie, *et al.*, "Entangled photons enabled time-frequency-resolved coherent Raman spectroscopy and applications to electronic coherences at femtosecond scale," *Light: Sci. Appl.* **11**, 274 (2022).

20. D. A. Kalashnikov, A. V. Paterova, S. P. Kulik, *et al.*, "Infrared spectroscopy with visible light," *Nat. Photonics* **10**, 98–101 (2016).
21. S. K. Lee, T. H. Yoon, and M. Cho, "Interferometric quantum spectroscopy with undetected photons via distinguishability modulation," *Opt. Express* **27**, 14853–14870 (2019).
22. J. J. Fan, Z.-Y. J. Ou, and Z. Zhang, "Entangled photons enabled ultrafast stimulated Raman spectroscopy for molecular dynamics," *arXiv*, (2023).
23. Y. Fujihashi, K. Miwa, M. Higashi, *et al.*, "Probing exciton dynamics with spectral selectivity through the use of quantum entangled photons," *J. Chem. Phys.* **159**, 114201 (2023).
24. O. Roslyak, C. A. Marx, and S. Mukamel, "Nonlinear spectroscopy with entangled photons: manipulating quantum pathways of matter," *Phys. Rev. A* **79**, 033832 (2009).
25. O. Roslyak and S. Mukamel, "Multidimensional pump-probe spectroscopy with entangled twin-photon states," *Phys. Rev. A* **79**, 063409 (2009).
26. S. Mukamel and K. E. Dorfman, "Nonlinear fluctuations and dissipation in matter revealed by quantum light," *Phys. Rev. A* **91**, 053844 (2015).
27. M. G. Raymer, A. H. Marcus, J. R. Widom, *et al.*, "Entangled photon-pair two-dimensional fluorescence spectroscopy (EPP-2DFS)," *J. Phys. Chem. B* **117**, 15559–15575 (2013).
28. S. Asban, V. Y. Chernyak, and S. Mukamel, "Nonlinear quantum interferometric spectroscopy with entangled photon pairs," *J. Chem. Phys.* **156**, 094202 (2022).
29. K. E. Dorfman, F. Schlawin, and S. Mukamel, "Stimulated Raman spectroscopy with entangled light: enhanced resolution and pathway selection," *J. Phys. Chem. Lett.* **5**, 2843–2849 (2014).
30. S. Asban and S. Mukamel, "Distinguishability and "which pathway" information in multidimensional interferometric spectroscopy with a single entangled photon-pair," *Sci. Adv.* **7**, eabj4566 (2021).
31. M. Kizmann, H. K. Yadalam, V. Y. Chernyak, *et al.*, "Quantum interferometry and pathway selectivity in the nonlinear response of photosynthetic excitons," *Proc. Natl. Acad. Sci.* **120**, e2304737120 (2023).
32. H. K. Yadalam, M. Kizmann, J. R. Rouxel, *et al.*, "Quantum interferometric pathway selectivity in difference-frequency-generation spectroscopy," *J. Phys. Chem. Lett.* **14**, 10803–10809 (2023).
33. Y. Fujihashi, A. Ishizaki, and R. Shimizu, "Pathway selectivity in time-resolved spectroscopy using two-photon coincidence counting with quantum entangled photons," *J. Chem. Phys.* **160**, 104201 (2024).
34. Z. Wu, P. Wang, T. Wang, *et al.*, "Selective detection of dynamics-complete set of correlations via quantum channels," *Phys. Rev. Lett.* **132**, 200802 (2024).
35. S. Mukamel, "Superoperator representation of nonlinear response: Unifying quantum field and mode coupling theories," *Phys. Rev. E* **68**, 021111 (2003).
36. S. Mukamel, "Partially-time-ordered Schwinger-Keldysh loop expansion of coherent nonlinear optical susceptibilities," *Phys. Rev. A* **77**, 023801 (2008).
37. Z. Y. Ou, L. J. Wang, and L. Mandel, "Vacuum effects on interference in two-photon down conversion," *Phys. Rev. A* **40**, 1428–1435 (1989).
38. Z. Y. Ou, L. J. Wang, X. Y. Zou, *et al.*, "Evidence for phase memory in two-photon down conversion through entanglement with the vacuum," *Phys. Rev. A* **41**, 566–568 (1990).
39. H. P. Yuen and J. H. Shapiro, "Generation and detection of two-photon coherent states in degenerate four-wave mixing," *Opt. Lett.* **4**, 334–336 (1979).
40. R. E. Slusher, L. W. Hollberg, B. Yurke, *et al.*, "Observation of squeezed states generated by four-wave mixing in an optical cavity," *Phys. Rev. Lett.* **55**, 2409–2412 (1985).
41. R. M. Shelby, M. D. Levenson, S. H. Perlmutter, *et al.*, "Broad-band parametric deamplification of quantum noise in an optical fiber," *Phys. Rev. Lett.* **57**, 691–694 (1986).
42. M. Fiorentino, P. L. Voss, J. E. Sharping, *et al.*, "All-fiber photon-pair source for quantum communications," *IEEE Photonics Technol. Lett.* **14**, 983–985 (2002).
43. K. Garay-Palmett, H. McGuinness, O. Cohen, *et al.*, "Photon pair-state preparation with tailored spectral properties by spontaneous four-wave mixing in photonic-crystal fiber," *Opt. Express* **15**, 14870–14886 (2007).
44. C. McKinstrie, J. Christensen, K. Rottwitz, *et al.*, "Generation of two-temporal-mode photon states by vector four-wave mixing," *Opt. Express* **25**, 20877–20893 (2017).
45. C. A. Marx, U. Harbola, and S. Mukamel, "Nonlinear optical spectroscopy of single, few, and many molecules: Nonequilibrium Green's function QED approach," *Phys. Rev. A* **77**, 022110 (2008).
46. S. Mukamel, "Communication: The origin of many-particle signals in nonlinear optical spectroscopy of non-interacting particles," *J. Chem. Phys.* **145**, 041102 (2016).
47. K. Bennett, V. Y. Chernyak, and S. Mukamel, "Discriminating cascading processes in nonlinear optics: A QED analysis based on their molecular and geometric origin," *Phys. Rev. A* **95**, 033840 (2017).
48. O. Roslyak and S. Mukamel, "A unified description of sum frequency generation, parametric down conversion and two-photon fluorescence," *Mol. Phys.* **107**, 265–280 (2009).
49. S. Biswas, J. Kim, X. Zhang, *et al.*, "Coherent two-dimensional and broadband electronic spectroscopies," *Chem. Rev.* **122**, 4257–4321 (2022).
50. D. Abramavicius, L. Valkunas, and S. Mukamel, "Transport and correlated fluctuations in the nonlinear optical response of excitons," *Europhys. Lett.* **80**, 17005 (2007).
51. V. May and O. Kühn, *Charge and Energy Transfer Dynamics In Molecular Systems* (John Wiley & Sons, 2023).
52. H. Van Amerongen, R. Van Grondelle, L. Valkunas, *et al.*, *Photosynthetic Excitons* (World Scientific, 2000).
53. M. Schröter, S. D. Ivanov, J. Schulze, *et al.*, "Exciton–vibrational coupling in the dynamics and spectroscopy of Frenkel excitons in molecular aggregates," *Phys. Rep.* **567**, 1–78 (2015).
54. Y. Tanimura and R. Kubo, "Time evolution of a quantum system in contact with a nearly Gaussian-Markoffian noise bath," *J. Phys. Soc. Jpn.* **58**, 101–114 (1989).
55. Y. Tanimura and S. Mukamel, "Real-time path-integral approach to quantum coherence and dephasing in nonadiabatic transitions and nonlinear optical response," *Phys. Rev. E* **47**, 118–136 (1993).
56. Y. Tanimura, "Stochastic Liouville, Langevin, Fokker–Planck, and master equation approaches to quantum dissipative systems," *J. Phys. Soc. Jpn.* **75**, 082001 (2006).
57. Y. Tanimura, "Numerically "exact" approach to open quantum dynamics: The hierarchical equations of motion (HEOM)," *J. Chem. Phys.* **153**, 020901 (2020).
58. L. Chen, R. Zheng, Q. Shi, *et al.*, "Two-dimensional electronic spectra from the hierarchical equations of motion method: Application to model dimers," *J. Chem. Phys.* **132**, 024505 (2010).
59. T. A. Oliver, N. H. Lewis, and G. R. Fleming, "Correlating the motion of electrons and nuclei with two-dimensional electronic–vibrational spectroscopy," *Proc. Natl. Acad. Sci.* **111**, 10061–10066 (2014).
60. M. Cho and G. R. Fleming, "Two-dimensional electronic–vibrational spectroscopy reveals cross-correlation between solvation dynamics and vibrational spectral diffusion," *J. Phys. Chem. B* **124**, 11222–11235 (2020).



## Ultrafast four-wave-mixing spectroscopy with two vacuum fields and coincidence-double-heterodyne detection: supplement

**HARI KUMAR YADALAM**,<sup>1,2,3</sup>  **MATTHIAS KIZMANN**,<sup>1,2,4</sup>  **AND**  
**SHAUL MUKAMEL**<sup>1,2,5</sup>,

<sup>1</sup>*Department of Chemistry, University of California, Irvine, California 92614, USA*

<sup>2</sup>*Department of Physics and Astronomy, University of California, Irvine, California 92614, USA*

<sup>3</sup>*hyadalam@uci.edu*

<sup>4</sup>*mkizmann@uci.edu*

<sup>5</sup>*smukamel@uci.edu*

---

This supplement published with Optica Publishing Group on 2 October 2024 by The Authors under the terms of the [Creative Commons Attribution 4.0 License](https://creativecommons.org/licenses/by/4.0/) in the format provided by the authors and unedited. Further distribution of this work must maintain attribution to the author(s) and the published article's title, journal citation, and DOI.

Supplement DOI: <https://doi.org/10.6084/m9.figshare.26841046>

Parent Article DOI: <https://doi.org/10.1364/OPTICAQ.523848>

# Supplementary: Ultrafast Four-Wave-Mixing Spectroscopy with two vacuum fields and Coincidence-Double-Heterodyne detection

Hari Kumar Yadalam,<sup>1,2,\*</sup> Matthias Kizmann,<sup>1,2,†</sup> and Shaul Mukamel<sup>1,2,‡</sup>

<sup>1</sup>*Department of Chemistry, University of California, Irvine, CA 92614, USA*

<sup>2</sup>*Department of Physics and Astronomy, University of California, Irvine, CA 92614, USA*

## I. RULES FOR READING LADDER DIAGRAMS IN THE TIME DOMAIN

The following rules are used for translating ladder diagrams to the field and matter correlation functions [1].

- Time flows from bottom to top. Usually, the initial time is  $-\infty$ , and the final time is  $t$ .
- Left and right strands, respectively, correspond to the ket and bra of the matter-field density matrix.
- Each matter-field interaction occurring at a definite time is represented by various arrows, as discussed below.
- Each matter-field interaction is represented by an arrow, either on the left (left operators) or the right (right operators) at distinct times, indicated by the end points of inward pointing or starting points of outward pointing arrows.
- Within the rotating wave approximation, the interaction picture matter-field coupling Liouvillian is given as,

$$\mathcal{L}_{mf}(t) = -i \left[ \left( \mathcal{E}_L^\dagger(t) \cdot V_L(t) + V_L^\dagger(t) \cdot \mathcal{E}_L(t) \right) - \left( \mathcal{E}_R^\dagger(t) \cdot V_R(t) + V_R^\dagger(t) \cdot \mathcal{E}_R(t) \right) \right].$$

Clearly, in the rotating wave approximation, absorption (emission) of a photon involves excitation (de-excitation) in the matter.

Each term in the above matter-field interaction Liouvillian is represented by a distinct arrow,

$$\begin{array}{l} \text{Inward pointing arrow on the ket side} \\ \text{Outward pointing arrow on the ket side} \\ \text{Inward pointing arrow on the bra side} \\ \text{Outward pointing arrow on the bra side} \end{array} \left| \begin{array}{l} V_L^\dagger(t) \cdot \mathcal{E}_L(t) \\ \mathcal{E}_L^\dagger(t) \cdot V_L(t) \\ \mathcal{E}_R^\dagger(t) \cdot V_R(t) \\ V_R^\dagger(t) \cdot \mathcal{E}_R(t) \end{array} \right.$$

- Moreover, at the final observation time,  $t$ , as a convention, matter-field interaction is chosen to occur as an outward pointing arrow on the ket side. This can always be achieved by complex conjugation.
- Each ladder diagram translates into a correlation function, given by the product of alternating sequence of matter-field interaction terms represented by the arrows and free Liouville space evolution of matter and field degrees of freedom between two consecutive arrows.
- Finally, the above obtained correlation function must be multiplied by  $(-i)^{n_i+n_r}(-1)^{n_r}$  to get the final expression corresponding to the diagram. Here  $n_{l/r}$  are the number of interactions on the ket/bra side of the diagram.

## II. DOUBLE HETERODYNE DETECTION FOR ULTRAFAST FOUR WAVE MIXING SPECTROSCOPIES

To compute the four-wave mixing signals, we expand the coincidence signal,

$$\mathcal{S}_{DH} = 2 \left[ \prod_{i=3,4} \frac{1}{2\pi c_i c_i} \right] \text{Re} \int_{-\infty}^{+\infty} \int_{-\infty}^{+\infty} dt_4 dt_3 \left[ \langle \mathcal{T} \vec{E}_4^*(t_4) \cdot \vec{\mathcal{E}}_{4L}(t_4) \vec{E}_3^*(t_3) \cdot \vec{\mathcal{E}}_{3L}(t_3) \rangle - \langle \mathcal{T} \vec{E}_4^*(t_4) \cdot \vec{\mathcal{E}}_{4L}(t_4) \vec{\mathcal{E}}_{3R}^\dagger(t_3) \cdot \vec{E}_3(t_3) \rangle \right], \quad (1)$$

to fourth order in the system-field interaction. This gives,

\* hyadalam@uci.edu

† mkizmann@uci.edu

‡ smukamel@uci.edu

$$\mathcal{S}_{\mathcal{DH}} = 2 \left[ \prod_{i=3,4} \frac{1}{2\pi c_i c_i} \right] \frac{1}{4! \hbar^4} \text{Re} \int_{-\infty}^{+\infty} \cdots \int_{-\infty}^{+\infty} dt_{\bar{4}} dt_{\bar{3}} dt_4 \cdots dt_1 \left[ \langle \mathcal{T} \vec{E}_{\bar{4}}^*(t_{\bar{4}}) \cdot \vec{\mathcal{E}}_{4L}(t_{\bar{4}}) \vec{E}_{\bar{3}}^*(t_{\bar{3}}) \cdot \vec{\mathcal{E}}_{3L}(t_{\bar{3}}) \prod_{n=1}^4 H_{sf-}(t_n) \rangle_0 - \langle \mathcal{T} \vec{E}_{\bar{4}}^*(t_{\bar{4}}) \cdot \vec{\mathcal{E}}_{4L}(t_{\bar{4}}) \vec{\mathcal{E}}_{3R}^\dagger(t_{\bar{3}}) \cdot \vec{E}_{\bar{3}}(t_{\bar{3}}) \prod_{n=1}^4 H_{sf-}(t_n) \rangle_0 \right]. \quad (2)$$

Here  $\langle \cdots \rangle_0$  stands for expectation value with respect to the uncorrelated initial system and field state. In the above equation, upon expanding  $H_{sf-}(t)$ , we find that each term has  $2^{10}$  contributions, as each  $H_{sf-}$  contributes four terms (hence  $4^4$  for four  $H_{sf-}$  terms) and for each of the four terms, electric field can come from one of the four pulses (hence  $2^8 \times 2^2$  terms). These  $2^{10}$  terms can be grouped as  $2^9$  terms and their complex conjugates.

In conventional four-wave mixing spectroscopies, only terms arising from first-order interaction with each of the pulses are retained. Furthermore, for the system initially in the electronic ground state, and assuming the pulses are temporally well separated, i.e., arrive at the sample in the sequence  $1, \dots, 4$ , we find that only two terms contribute to the first term in Eq. (2) and six contribute to the second term. This gives,

$$\begin{aligned} \mathcal{S}_{\mathcal{DH}} = & \frac{2}{\hbar^4} \left[ \prod_{i=3,4} \frac{1}{2\pi c_i c_i} \right] \text{Re} \int_{-\infty}^{+\infty} dt_{\bar{4}} \int_{-\infty}^{+\infty} dt_{\bar{3}} \int_{-\infty}^{+\infty} dt_4 \int_{-\infty}^{t_4} dt_3 \int_{-\infty}^{t_3} dt_2 \int_{-\infty}^{t_2} dt_1 \\ & \int_{\mathbf{r}_4 \in \text{sample}} d^3 \mathbf{r}_4 \cdots \int_{\mathbf{r}_1 \in \text{sample}} d^3 \mathbf{r}_1 \sum_{n_4, \dots, n_1=x,y,z} \\ & e^{-i(\mathbf{k}_4 \cdot \mathbf{r}_4 + \mathbf{k}_3 \cdot \mathbf{r}_3 - \mathbf{k}_2 \cdot \mathbf{r}_2 - \mathbf{k}_1 \cdot \mathbf{r}_1)} \\ & \left[ \langle \mathcal{V}_L^{n_4}(\mathbf{r}_4, t_4) \mathcal{V}_L^{n_3}(\mathbf{r}_3, t_3) \mathcal{V}_L^{n_2 \dagger}(\mathbf{r}_2, t_2) \mathcal{V}_L^{n_1 \dagger}(\mathbf{r}_1, t_1) \rangle_s \langle \mathcal{T} \vec{E}_{\bar{4}}^*(t_{\bar{4}}) \cdot \vec{\mathcal{E}}_{4L}(t_{\bar{4}}) \vec{E}_{\bar{3}}^*(t_{\bar{3}}) \cdot \vec{\mathcal{E}}_{3L}(t_{\bar{3}}) \mathcal{E}_{4L}^{n_4 \dagger}(t_4) \mathcal{E}_{3L}^{n_3 \dagger}(t_3) \mathcal{E}_{2L}^{n_2}(t_2) \mathcal{E}_{1L}^{n_1}(t_1) \rangle_f \right. \\ & - \langle \mathcal{V}_L^{n_4}(\mathbf{r}_4, t_4) \mathcal{V}_R^{n_3}(\mathbf{r}_3, t_3) \mathcal{V}_L^{n_2 \dagger}(\mathbf{r}_2, t_2) \mathcal{V}_L^{n_1 \dagger}(\mathbf{r}_1, t_1) \rangle_s \langle \mathcal{T} \vec{E}_{\bar{4}}^*(t_{\bar{4}}) \cdot \vec{\mathcal{E}}_{4L}(t_{\bar{4}}) \vec{E}_{\bar{3}}^*(t_{\bar{3}}) \cdot \vec{\mathcal{E}}_{3L}(t_{\bar{3}}) \mathcal{E}_{4L}^{n_4 \dagger}(t_4) \mathcal{E}_{3R}^{n_3 \dagger}(t_3) \mathcal{E}_{2L}^{n_2}(t_2) \mathcal{E}_{1L}^{n_1}(t_1) \rangle_f \left. \right] \\ & - e^{-i(\mathbf{k}_4 \cdot \mathbf{r}_4 - \mathbf{k}_3 \cdot \mathbf{r}_3 + \mathbf{k}_2 \cdot \mathbf{r}_2 - \mathbf{k}_1 \cdot \mathbf{r}_1)} \\ & \left[ \langle \mathcal{V}_L^{n_4}(\mathbf{r}_4, t_4) \mathcal{V}_R^{n_3 \dagger}(\mathbf{r}_3, t_3) \mathcal{V}_R^{n_2}(\mathbf{r}_2, t_2) \mathcal{V}_L^{n_1 \dagger}(\mathbf{r}_1, t_1) \rangle_s \langle \mathcal{T} \vec{E}_{\bar{4}}^*(t_{\bar{4}}) \cdot \vec{\mathcal{E}}_{4L}(t_{\bar{4}}) \vec{\mathcal{E}}_{3R}^\dagger(t_{\bar{3}}) \cdot \vec{E}_{\bar{3}}(t_{\bar{3}}) \mathcal{E}_{4L}^{n_4 \dagger}(t_4) \mathcal{E}_{3R}^{n_3}(t_3) \mathcal{E}_{2R}^{n_2 \dagger}(t_2) \mathcal{E}_{1L}^{n_1}(t_1) \rangle_f \right. \\ & - \langle \mathcal{V}_L^{n_4}(\mathbf{r}_4, t_4) \mathcal{V}_L^{n_3 \dagger}(\mathbf{r}_3, t_3) \mathcal{V}_R^{n_2}(\mathbf{r}_2, t_2) \mathcal{V}_L^{n_1 \dagger}(\mathbf{r}_1, t_1) \rangle_s \langle \mathcal{T} \vec{E}_{\bar{4}}^*(t_{\bar{4}}) \cdot \vec{\mathcal{E}}_{4L}(t_{\bar{4}}) \vec{\mathcal{E}}_{3R}^\dagger(t_{\bar{3}}) \cdot \vec{E}_{\bar{3}}(t_{\bar{3}}) \mathcal{E}_{4L}^{n_4 \dagger}(t_4) \mathcal{E}_{3L}^{n_3}(t_3) \mathcal{E}_{2R}^{n_2 \dagger}(t_2) \mathcal{E}_{1L}^{n_1}(t_1) \rangle_f \\ & + \langle \mathcal{V}_L^{n_4}(\mathbf{r}_4, t_4) \mathcal{V}_L^{n_3 \dagger}(\mathbf{r}_3, t_3) \mathcal{V}_L^{n_2}(\mathbf{r}_2, t_2) \mathcal{V}_L^{n_1 \dagger}(\mathbf{r}_1, t_1) \rangle_s \langle \mathcal{T} \vec{E}_{\bar{4}}^*(t_{\bar{4}}) \cdot \vec{\mathcal{E}}_{4L}(t_{\bar{4}}) \vec{\mathcal{E}}_{3R}^\dagger(t_{\bar{3}}) \cdot \vec{E}_{\bar{3}}(t_{\bar{3}}) \mathcal{E}_{4L}^{n_4 \dagger}(t_4) \mathcal{E}_{3L}^{n_3}(t_3) \mathcal{E}_{2L}^{n_2 \dagger}(t_2) \mathcal{E}_{1L}^{n_1}(t_1) \rangle_f \left. \right] \\ & - e^{-i(\mathbf{k}_4 \cdot \mathbf{r}_4 - \mathbf{k}_3 \cdot \mathbf{r}_3 - \mathbf{k}_2 \cdot \mathbf{r}_2 + \mathbf{k}_1 \cdot \mathbf{r}_1)} \\ & \left[ \langle \mathcal{V}_L^{n_4}(\mathbf{r}_4, t_4) \mathcal{V}_R^{n_3 \dagger}(\mathbf{r}_3, t_3) \mathcal{V}_L^{n_2 \dagger}(\mathbf{r}_2, t_2) \mathcal{V}_R^{n_1}(\mathbf{r}_1, t_1) \rangle_s \langle \mathcal{T} \vec{E}_{\bar{4}}^*(t_{\bar{4}}) \cdot \vec{\mathcal{E}}_{4L}(t_{\bar{4}}) \vec{\mathcal{E}}_{3R}^\dagger(t_{\bar{3}}) \cdot \vec{E}_{\bar{3}}(t_{\bar{3}}) \mathcal{E}_{4L}^{n_4 \dagger}(t_4) \mathcal{E}_{3R}^{n_3}(t_3) \mathcal{E}_{2L}^{n_2}(t_2) \mathcal{E}_{1R}^{n_1 \dagger}(t_1) \rangle_f \right. \\ & - \langle \mathcal{V}_L^{n_4}(\mathbf{r}_4, t_4) \mathcal{V}_L^{n_3 \dagger}(\mathbf{r}_3, t_3) \mathcal{V}_L^{n_2 \dagger}(\mathbf{r}_2, t_2) \mathcal{V}_R^{n_1}(\mathbf{r}_1, t_1) \rangle_s \langle \mathcal{T} \vec{E}_{\bar{4}}^*(t_{\bar{4}}) \cdot \vec{\mathcal{E}}_{4L}(t_{\bar{4}}) \vec{\mathcal{E}}_{3R}^\dagger(t_{\bar{3}}) \cdot \vec{E}_{\bar{3}}(t_{\bar{3}}) \mathcal{E}_{4L}^{n_4 \dagger}(t_4) \mathcal{E}_{3L}^{n_3}(t_3) \mathcal{E}_{2L}^{n_2}(t_2) \mathcal{E}_{1R}^{n_1 \dagger}(t_1) \rangle_f \\ & + \langle \mathcal{V}_L^{n_4}(\mathbf{r}_4, t_4) \mathcal{V}_L^{n_3 \dagger}(\mathbf{r}_3, t_3) \mathcal{V}_R^{n_2 \dagger}(\mathbf{r}_2, t_2) \mathcal{V}_R^{n_1}(\mathbf{r}_1, t_1) \rangle_s \langle \mathcal{T} \vec{E}_{\bar{4}}^*(t_{\bar{4}}) \cdot \vec{\mathcal{E}}_{4L}(t_{\bar{4}}) \vec{\mathcal{E}}_{3R}^\dagger(t_{\bar{3}}) \cdot \vec{E}_{\bar{3}}(t_{\bar{3}}) \mathcal{E}_{4L}^{n_4 \dagger}(t_4) \mathcal{E}_{3L}^{n_3}(t_3) \mathcal{E}_{2R}^{n_2 \dagger}(t_2) \mathcal{E}_{1R}^{n_1 \dagger}(t_1) \rangle_f \left. \right]. \quad (3) \end{aligned}$$

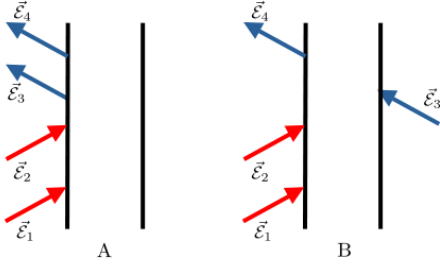
Here  $\langle \cdots \rangle_s$  and  $\langle \cdots \rangle_f$  are, respectively, sample and field multipoint correlation functions. The sample correlation functions entering in each of the terms in Eq. (3) are represented by the ladder diagrams shown in Fig. (1). Where the two terms appearing with  $e^{-i(\mathbf{k}_4 \cdot \mathbf{r}_4 + \mathbf{k}_3 \cdot \mathbf{r}_3 - \mathbf{k}_2 \cdot \mathbf{r}_2 - \mathbf{k}_1 \cdot \mathbf{r}_1)}$  are respectively represented

by Fig. (1.DQC). The three terms appearing with  $e^{-i(\mathbf{k}_4 \cdot \mathbf{r}_4 - \mathbf{k}_3 \cdot \mathbf{r}_3 + \mathbf{k}_2 \cdot \mathbf{r}_2 - \mathbf{k}_1 \cdot \mathbf{r}_1)}$  are respectively represented by Fig. (1.NRP). Finally, the three terms appearing with  $e^{-i(\mathbf{k}_4 \cdot \mathbf{r}_4 - \mathbf{k}_3 \cdot \mathbf{r}_3 - \mathbf{k}_2 \cdot \mathbf{r}_2 + \mathbf{k}_1 \cdot \mathbf{r}_1)}$  are respectively represented by Fig. (1.PE). Note that in Eq. (3), the sample four-point correlators represented by various diagrams in

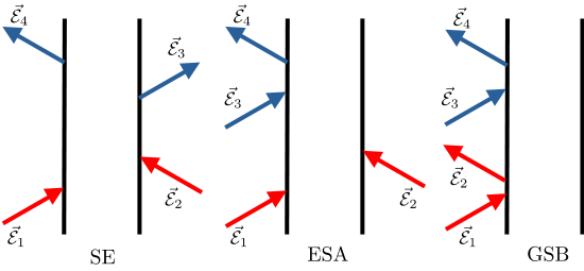
Fig. (1) are convolved with different field correlation functions. Since the ladder diagrams in Figs. (1.DQC.B, 1.NRP.ESA, 1.NRP.GSB, 1.PE.ESA & 1.PE.GSB), involve absorption of photons in pulse 3, either on the ket or the bra side, and as this pulse is initially in the vacuum state, these diagrams do not contribute to the signal. This can also be clearly seen from the respective field correlation function, which vanish for the initial state of the pulses,  $\mathcal{I} = 1, 2, \tilde{3}$  &  $\tilde{4}$ , given by,

$$|\Psi(-\infty)\rangle = e^{i\sum_{i\in\mathcal{I}}\int_{-\infty}^{+\infty}\frac{d\omega}{2\pi}[\alpha_i(\omega)a_{i\epsilon_i}^\dagger(\omega)-\alpha_i^*(\omega)a_{i\epsilon_i}(\omega)]}|\emptyset\rangle.$$

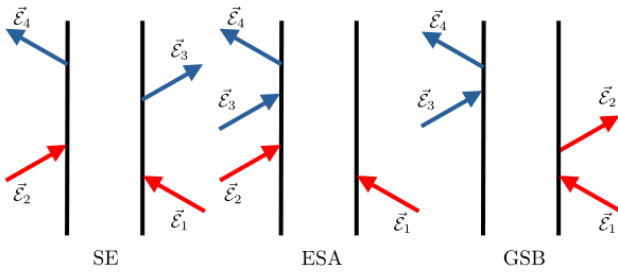
Finally, decoupling the field correlation functions for various pulses and substituting the field operators corresponding to pulses 1 & 2 with their respective classical field envelopes,  $\vec{E}_i(t_i) = \langle\Psi(-\infty)|\vec{\mathcal{E}}_i(t_i)|\Psi(-\infty)\rangle$ , we get,



$$\text{DQC: } \mathbf{k}_4 + \mathbf{k}_3 = \mathbf{k}_2 + \mathbf{k}_1$$



$$\text{NRP: } \mathbf{k}_4 - \mathbf{k}_3 = -\mathbf{k}_2 + \mathbf{k}_1$$



$$\text{PE: } \mathbf{k}_4 - \mathbf{k}_3 = \mathbf{k}_2 - \mathbf{k}_1$$

FIG. 1. Ladder diagrams contributing to the three dominant phase matching directions in the four-wave mixing spectroscopies: (i) Double Quantum Coherence Signal (**DQC**:  $\mathbf{k}_4 + \mathbf{k}_3 = \mathbf{k}_2 + \mathbf{k}_1$ ), (ii) Non-rephasing signal (**NRP**:  $\mathbf{k}_4 - \mathbf{k}_3 = -\mathbf{k}_2 + \mathbf{k}_1$ ) and (iii) Photon-echo signal (**PE**:  $\mathbf{k}_4 - \mathbf{k}_3 = \mathbf{k}_2 - \mathbf{k}_1$ ).

$$\begin{aligned}
\mathcal{S}_{\mathcal{DH}} = & \frac{2}{\hbar^4} \text{Re} \int_{-\infty}^{+\infty} dt_4 \int_{-\infty}^{t_4} dt_3 \int_{-\infty}^{t_3} dt_2 \int_{-\infty}^{t_2} dt_1 \int_{\mathbf{r}_4 \in \text{sample}} d^3 \mathbf{r}_4 \cdots \int_{\mathbf{r}_1 \in \text{sample}} d^3 \mathbf{r}_1 \sum_{n_4, \dots, n_1=x,y,z} \\
& e^{-i(\mathbf{k}_4 \cdot \mathbf{r}_4 + \mathbf{k}_3 \cdot \mathbf{r}_3 - \mathbf{k}_2 \cdot \mathbf{r}_2 - \mathbf{k}_1 \cdot \mathbf{r}_1)} \langle \mathcal{V}_L^{n_4}(\mathbf{r}_4, t_4) \mathcal{V}_L^{n_3}(\mathbf{r}_3, t_3) \mathcal{V}_L^{n_2 \dagger}(\mathbf{r}_2, t_2) \mathcal{V}_L^{n_1 \dagger}(\mathbf{r}_1, t_1) \rangle_s E_4^{n_4^*}(t_4) E_3^{n_3^*}(t_3) E_2^{n_2}(t_2) E_1^{n_1}(t_1) \\
& - e^{-i(\mathbf{k}_4 \cdot \mathbf{r}_4 - \mathbf{k}_3 \cdot \mathbf{r}_3 + \mathbf{k}_2 \cdot \mathbf{r}_2 - \mathbf{k}_1 \cdot \mathbf{r}_1)} \langle \mathcal{V}_L^{n_4}(\mathbf{r}_4, t_4) \mathcal{V}_R^{n_3 \dagger}(\mathbf{r}_3, t_3) \mathcal{V}_R^{n_2}(\mathbf{r}_2, t_2) \mathcal{V}_L^{n_1 \dagger}(\mathbf{r}_1, t_1) \rangle_s E_4^{n_4^*}(t_4) E_3^{n_3}(t_3) E_2^{n_2^*}(t_2) E_1^{n_1}(t_1) \\
& - e^{-i(\mathbf{k}_4 \cdot \mathbf{r}_4 - \mathbf{k}_3 \cdot \mathbf{r}_3 - \mathbf{k}_2 \cdot \mathbf{r}_2 + \mathbf{k}_1 \cdot \mathbf{r}_1)} \langle \mathcal{V}_L^{n_4}(\mathbf{r}_4, t_4) \mathcal{V}_R^{n_3 \dagger}(\mathbf{r}_3, t_3) \mathcal{V}_L^{n_2 \dagger}(\mathbf{r}_2, t_2) \mathcal{V}_R^{n_1}(\mathbf{r}_1, t_1) \rangle_s E_4^{n_4^*}(t_4) E_3^{n_3}(t_3) E_2^{n_2}(t_2) E_1^{n_1^*}(t_1).
\end{aligned} \tag{4}$$

For the dilute sample with a collection of identical non-interacting molecules, which is considered here, the above

signal can be expressed in terms of single-molecule response functions as follows,

$$\begin{aligned}
\mathcal{S}_{\mathcal{DH}} = & \frac{2}{\hbar^4} \text{Re} \int_{-\infty}^{+\infty} dt_4 \int_{-\infty}^{t_4} dt_3 \int_{-\infty}^{t_3} dt_2 \int_{-\infty}^{t_2} dt_1 \sum_{n_4, \dots, n_1=x,y,z} \\
& \left( \Phi(\mathbf{k}_4 + \mathbf{k}_3 - \mathbf{k}_2 - \mathbf{k}_1) \right. \\
& \left[ \langle \mathcal{V}_L^{n_4}(t_4) \mathcal{V}_L^{n_3}(t_3) \mathcal{V}_L^{n_2 \dagger}(t_2) \mathcal{V}_L^{n_1 \dagger}(t_1) \rangle_s - \langle \mathcal{V}_L^{n_4}(t_4) \mathcal{V}_L^{n_2 \dagger}(t_2) \rangle_s \langle \mathcal{V}_L^{n_3}(t_3) \mathcal{V}_L^{n_1 \dagger}(t_1) \rangle_s - \langle \mathcal{V}_L^{n_4}(t_4) \mathcal{V}_L^{n_1 \dagger}(t_1) \rangle_s \langle \mathcal{V}_L^{n_3}(t_3) \mathcal{V}_L^{n_2 \dagger}(t_2) \rangle_s \right] \\
& + \Phi(\mathbf{k}_4 - \mathbf{k}_2) \Phi(\mathbf{k}_3 - \mathbf{k}_1) \langle \mathcal{V}_L^{n_4}(t_4) \mathcal{V}_L^{n_2 \dagger}(t_2) \rangle_s \langle \mathcal{V}_L^{n_3}(t_3) \mathcal{V}_L^{n_1 \dagger}(t_1) \rangle_s \\
& + \Phi(\mathbf{k}_4 - \mathbf{k}_1) \Phi(\mathbf{k}_3 - \mathbf{k}_2) \langle \mathcal{V}_L^{n_4}(t_4) \mathcal{V}_L^{n_1 \dagger}(t_1) \rangle_s \langle \mathcal{V}_L^{n_3}(t_3) \mathcal{V}_L^{n_2 \dagger}(t_2) \rangle_s \left. \right) E_4^{n_4^*}(t_4) E_3^{n_3^*}(t_3) E_2^{n_2}(t_2) E_1^{n_1}(t_1) \\
& - \left( \Phi(\mathbf{k}_4 - \mathbf{k}_3 + \mathbf{k}_2 - \mathbf{k}_1) \left[ \langle \mathcal{V}_L^{n_4}(t_4) \mathcal{V}_R^{n_3 \dagger}(t_3) \mathcal{V}_R^{n_2}(t_2) \mathcal{V}_L^{n_1 \dagger}(t_1) \rangle_s - \langle \mathcal{V}_L^{n_4}(t_4) \mathcal{V}_L^{n_1 \dagger}(t_1) \rangle_s \langle \mathcal{V}_R^{n_3 \dagger}(t_3) \mathcal{V}_R^{n_2}(t_2) \rangle_s \right] \right. \\
& + \Phi(\mathbf{k}_4 - \mathbf{k}_1) \Phi(-\mathbf{k}_3 + \mathbf{k}_2) \langle \mathcal{V}_L^{n_4}(t_4) \mathcal{V}_L^{n_1 \dagger}(t_1) \rangle_s \langle \mathcal{V}_R^{n_3 \dagger}(t_3) \mathcal{V}_R^{n_2}(t_2) \rangle_s \left. \right) E_4^{n_4^*}(t_4) E_3^{n_3}(t_3) E_2^{n_2^*}(t_2) E_1^{n_1}(t_1) \\
& - \left( \Phi(\mathbf{k}_4 - \mathbf{k}_3 - \mathbf{k}_2 + \mathbf{k}_1) \left[ \langle \mathcal{V}_L^{n_4}(t_4) \mathcal{V}_R^{n_3 \dagger}(t_3) \mathcal{V}_L^{n_2 \dagger}(t_2) \mathcal{V}_R^{n_1}(t_1) \rangle_s - \langle \mathcal{V}_L^{n_4}(t_4) \mathcal{V}_L^{n_2 \dagger}(t_2) \rangle_s \langle \mathcal{V}_R^{n_3 \dagger}(t_3) \mathcal{V}_R^{n_1}(t_1) \rangle_s \right] \right. \\
& + \Phi(\mathbf{k}_4 - \mathbf{k}_2) \Phi(-\mathbf{k}_3 + \mathbf{k}_1) \langle \mathcal{V}_L^{n_4}(t_4) \mathcal{V}_L^{n_2 \dagger}(t_2) \rangle_s \langle \mathcal{V}_R^{n_3 \dagger}(t_3) \mathcal{V}_R^{n_1}(t_1) \rangle_s \left. \right) E_4^{n_4^*}(t_4) E_3^{n_3}(t_3) E_2^{n_2}(t_2) E_1^{n_1^*}(t_1).
\end{aligned} \tag{5}$$

Here,  $\Phi(\mathbf{k}) = \sum_m e^{-i\mathbf{k} \cdot \mathbf{r}_m}$  stands for the phase matching function, where the sum runs over  $N$  molecules in the sample that interact with all four pulses 1, 2, 3 & 4. For homogeneous samples this simplifies to  $\Phi(\mathbf{k}) = N \int_{\mathbf{r} \in \mathbf{V}^*} d^3 \mathbf{r} e^{-i\mathbf{k} \cdot \mathbf{r}}$ , where  $\mathbf{V}^*$  is the interaction volume. For sufficiently large transverse areas of pulses and large sample sizes, this further simplifies to  $\Phi(\mathbf{k}) = (2\pi)^3 N \delta^{(3)}(\mathbf{k})$ . Hence, the signal has two distinct contributions: (i) the single molecule contribution proportional to  $N$  and (ii) the two-molecule coherent contribution proportional to  $N^2$ . The two-molecule contribu-

tion is expressed in terms of a single molecule's two-point correlation functions, giving the same information as linear spectroscopies. Furthermore, for isotropic samples, the above signal has to be rotationally averaged to obtain the macroscopic signal. This rotational averaging has to be performed differently for the two contributions discussed above. For the linear in  $N$  contribution, the four-point correlation function of the molecule must be rotationally averaged, while for the  $N^2$  contribution, the two two-point correlation functions of molecules must be rotationally averaged separately. The rotationally averaged macroscopic signal [2] is finally given by

$$\begin{aligned}
\mathcal{S}_{\mathcal{DH}} = & \frac{2}{\hbar^4} \text{Re} \int_{-\infty}^{+\infty} dt_4 \int_{-\infty}^{t_4} dt_3 \int_{-\infty}^{t_3} dt_2 \int_{-\infty}^{t_2} dt_1 \sum_{n_4, \dots, n_1=x,y,z} \\
& \Phi(\mathbf{k}_4 + \mathbf{k}_3 - \mathbf{k}_2 - \mathbf{k}_1) \times \\
& [\langle \mathcal{V}_L^{n_4}(t_4) \mathcal{V}_L^{n_3}(t_3) \mathcal{V}_L^{n_2\dagger}(t_2) \mathcal{V}_L^{n_1\dagger}(t_1) \rangle_s - \langle \mathcal{V}_L^{n_4}(t_4) \mathcal{V}_L^{n_2\dagger}(t_2) \rangle_s \langle \mathcal{V}_L^{n_3}(t_3) \mathcal{V}_L^{n_1\dagger}(t_1) \rangle_s - \langle \mathcal{V}_L^{n_4}(t_4) \mathcal{V}_L^{n_1\dagger}(t_1) \rangle_s \langle \mathcal{V}_L^{n_3}(t_3) \mathcal{V}_L^{n_2\dagger}(t_2) \rangle_s] \\
& \times \mathcal{R}_{n_4, n_3, n_2, n_1}^T \begin{bmatrix} \vec{E}_4^*(t_4) \cdot \vec{E}_3^*(t_3) \vec{E}_2(t_2) \cdot \vec{E}_1(t_1) \\ \vec{E}_4^*(t_4) \cdot \vec{E}_2(t_2) \vec{E}_3^*(t_3) \cdot \vec{E}_1(t_1) \\ \vec{E}_4^*(t_4) \cdot \vec{E}_1(t_1) \vec{E}_3^*(t_3) \cdot \vec{E}_2(t_2) \end{bmatrix} \\
& - \Phi(\mathbf{k}_4 - \mathbf{k}_3 + \mathbf{k}_2 - \mathbf{k}_1) \times \\
& [\langle \mathcal{V}_L^{n_4}(t_4) \mathcal{V}_R^{n_3\dagger}(t_3) \mathcal{V}_R^{n_2}(t_2) \mathcal{V}_L^{n_1\dagger}(t_1) \rangle_s - \langle \mathcal{V}_L^{n_4}(t_4) \mathcal{V}_L^{n_1\dagger}(t_1) \rangle_s \langle \mathcal{V}_R^{n_3\dagger}(t_3) \mathcal{V}_R^{n_2}(t_2) \rangle_s] \\
& \times \mathcal{R}_{n_4, n_3, n_2, n_1}^T \begin{bmatrix} \vec{E}_4^*(t_4) \cdot \vec{E}_3(t_3) \vec{E}_2^*(t_2) \cdot \vec{E}_1(t_1) \\ \vec{E}_4^*(t_4) \cdot \vec{E}_2^*(t_2) \vec{E}_3(t_3) \cdot \vec{E}_1(t_1) \\ \vec{E}_4^*(t_4) \cdot \vec{E}_1(t_1) \vec{E}_3(t_3) \cdot \vec{E}_2^*(t_2) \end{bmatrix} \\
& - \Phi(\mathbf{k}_4 - \mathbf{k}_3 - \mathbf{k}_2 + \mathbf{k}_1) \\
& [\langle \mathcal{V}_L^{n_4}(t_4) \mathcal{V}_R^{n_3\dagger}(t_3) \mathcal{V}_L^{n_2\dagger}(t_2) \mathcal{V}_R^{n_1}(t_1) \rangle_s - \langle \mathcal{V}_L^{n_4}(t_4) \mathcal{V}_L^{n_2\dagger}(t_2) \rangle_s \langle \mathcal{V}_R^{n_3\dagger}(t_3) \mathcal{V}_R^{n_1}(t_1) \rangle_s] \\
& \times \mathcal{R}_{n_4, n_3, n_2, n_1}^T \begin{bmatrix} \vec{E}_4^*(t_4) \cdot \vec{E}_3(t_3) \vec{E}_2(t_2) \cdot \vec{E}_1^*(t_1) \\ \vec{E}_4^*(t_4) \cdot \vec{E}_2(t_2) \vec{E}_3(t_3) \cdot \vec{E}_1^*(t_1) \\ \vec{E}_4^*(t_4) \cdot \vec{E}_1^*(t_1) \vec{E}_3(t_3) \cdot \vec{E}_2(t_2) \end{bmatrix} \\
& + \frac{\Phi(\mathbf{k}_4 - \mathbf{k}_2) \Phi(\mathbf{k}_3 - \mathbf{k}_1)}{9} \langle \vec{\mathcal{V}}_L(t_4) \cdot \vec{\mathcal{V}}_L^\dagger(t_2) \rangle_s \langle \vec{\mathcal{V}}_L(t_3) \cdot \vec{\mathcal{V}}_L^\dagger(t_1) \rangle_s \vec{E}_4^*(t_4) \cdot \vec{E}_2(t_2) \vec{E}_3^*(t_3) \cdot \vec{E}_1(t_1) \\
& + \frac{\Phi(\mathbf{k}_4 - \mathbf{k}_1) \Phi(\mathbf{k}_3 - \mathbf{k}_2)}{9} \langle \vec{\mathcal{V}}_L(t_4) \cdot \vec{\mathcal{V}}_L^\dagger(t_1) \rangle_s \langle \vec{\mathcal{V}}_L(t_3) \cdot \vec{\mathcal{V}}_L^\dagger(t_2) \rangle_s \vec{E}_4^*(t_4) \cdot \vec{E}_1(t_1) \vec{E}_3^*(t_3) \cdot \vec{E}_2(t_2) \\
& - \frac{\Phi(\mathbf{k}_4 - \mathbf{k}_1) \Phi(-\mathbf{k}_3 + \mathbf{k}_2)}{9} \langle \vec{\mathcal{V}}_L(t_4) \cdot \vec{\mathcal{V}}_L^\dagger(t_1) \rangle_s \langle \vec{\mathcal{V}}_R^\dagger(t_3) \cdot \vec{\mathcal{V}}_R(t_2) \rangle_s \vec{E}_4^*(t_4) \cdot \vec{E}_1(t_1) \vec{E}_3(t_3) \cdot \vec{E}_2^*(t_2) \\
& - \frac{\Phi(\mathbf{k}_4 - \mathbf{k}_2) \Phi(-\mathbf{k}_3 + \mathbf{k}_1)}{9} \langle \vec{\mathcal{V}}_L(t_4) \cdot \vec{\mathcal{V}}_L^\dagger(t_2) \rangle_s \langle \vec{\mathcal{V}}_R^\dagger(t_3) \cdot \vec{\mathcal{V}}_R(t_1) \rangle_s \vec{E}_4^*(t_4) \cdot \vec{E}_2(t_2) \vec{E}_3(t_3) \cdot \vec{E}_1^*(t_1). \tag{6}
\end{aligned}$$

Here

$$\mathcal{R}_{n_4, n_3, n_2, n_1} = \frac{1}{30} \begin{bmatrix} 4\delta_{n_4 n_3} \delta_{n_2 n_1} - \delta_{n_4 n_2} \delta_{n_3 n_1} - \delta_{n_4 n_1} \delta_{n_3 n_2} \\ -\delta_{n_4 n_3} \delta_{n_2 n_1} + 4\delta_{n_4 n_2} \delta_{n_3 n_1} - \delta_{n_4 n_1} \delta_{n_3 n_2} \\ -\delta_{n_4 n_3} \delta_{n_2 n_1} - \delta_{n_4 n_2} \delta_{n_3 n_1} + 4\delta_{n_4 n_1} \delta_{n_3 n_2} \end{bmatrix}$$

Clearly, by avoiding collecting signals in the directions,  $\mathbf{k}_{4/3}$  identical to the incoming pulse central wave-vector

directions,  $\mathbf{k}_{2/1}$ , the uninteresting  $N^2$  contributions to the signal, the last four terms in Eq. (6), can be suppressed. This suppression can also be achieved by choosing the polarization of pulses 3&4 to be orthogonal to that of the pulses 1&2. For this sample irradiation and detection geometry, the signal becomes,

$$\begin{aligned}
\mathcal{S}_{\mathcal{DH}} = & \frac{2}{\hbar^4} \text{Re} \int_{-\infty}^{+\infty} dt_4 \int_{-\infty}^{t_4} dt_3 \int_{-\infty}^{t_3} dt_2 \int_{-\infty}^{t_2} dt_1 \sum_{n_4, \dots, n_1=x,y,z} \\
& \Phi(\mathbf{k}_4 + \mathbf{k}_3 - \mathbf{k}_2 - \mathbf{k}_1) \times \\
& [\langle \mathcal{V}_L^{n_4}(t_4) \mathcal{V}_L^{n_3}(t_3) \mathcal{V}_L^{n_2\dagger}(t_2) \mathcal{V}_L^{n_1\dagger}(t_1) \rangle_s - \langle \mathcal{V}_L^{n_4}(t_4) \mathcal{V}_L^{n_2\dagger}(t_2) \rangle_s \langle \mathcal{V}_L^{n_3}(t_3) \mathcal{V}_L^{n_1\dagger}(t_1) \rangle_s - \langle \mathcal{V}_L^{n_4}(t_4) \mathcal{V}_L^{n_1\dagger}(t_1) \rangle_s \langle \mathcal{V}_L^{n_3}(t_3) \mathcal{V}_L^{n_2\dagger}(t_2) \rangle_s] \\
& \times \mathcal{R}_{n_4, n_3, n_2, n_1}^T \begin{bmatrix} \vec{E}_4^*(t_4) \cdot \vec{E}_3^*(t_3) \vec{E}_2(t_2) \cdot \vec{E}_1(t_1) \\ \vec{E}_4^*(t_4) \cdot \vec{E}_2(t_2) \vec{E}_3^*(t_3) \cdot \vec{E}_1(t_1) \\ \vec{E}_4^*(t_4) \cdot \vec{E}_1(t_1) \vec{E}_3^*(t_3) \cdot \vec{E}_2(t_2) \end{bmatrix} \\
& - \Phi(\mathbf{k}_4 - \mathbf{k}_3 + \mathbf{k}_2 - \mathbf{k}_1) \times \\
& [\langle \mathcal{V}_L^{n_4}(t_4) \mathcal{V}_R^{n_3\dagger}(t_3) \mathcal{V}_R^{n_2}(t_2) \mathcal{V}_L^{n_1\dagger}(t_1) \rangle_s - \langle \mathcal{V}_L^{n_4}(t_4) \mathcal{V}_L^{n_1\dagger}(t_1) \rangle_s \langle \mathcal{V}_R^{n_3\dagger}(t_3) \mathcal{V}_R^{n_2}(t_2) \rangle_s] \\
& \times \mathcal{R}_{n_4, n_3, n_2, n_1}^T \begin{bmatrix} \vec{E}_4^*(t_4) \cdot \vec{E}_3(t_3) \vec{E}_2^*(t_2) \cdot \vec{E}_1(t_1) \\ \vec{E}_4^*(t_4) \cdot \vec{E}_2^*(t_2) \vec{E}_3(t_3) \cdot \vec{E}_1(t_1) \\ \vec{E}_4^*(t_4) \cdot \vec{E}_1(t_1) \vec{E}_3(t_3) \cdot \vec{E}_2^*(t_2) \end{bmatrix} \\
& - \Phi(\mathbf{k}_4 - \mathbf{k}_3 - \mathbf{k}_2 + \mathbf{k}_1) \times \\
& [\langle \mathcal{V}_L^{n_4}(t_4) \mathcal{V}_R^{n_3\dagger}(t_3) \mathcal{V}_L^{n_2\dagger}(t_2) \mathcal{V}_R^{n_1}(t_1) \rangle_s - \langle \mathcal{V}_L^{n_4}(t_4) \mathcal{V}_L^{n_2\dagger}(t_2) \rangle_s \langle \mathcal{V}_R^{n_3\dagger}(t_3) \mathcal{V}_R^{n_1}(t_1) \rangle_s] \\
& \times \mathcal{R}_{n_4, n_3, n_2, n_1}^T \begin{bmatrix} \vec{E}_4^*(t_4) \cdot \vec{E}_3(t_3) \vec{E}_2(t_2) \cdot \vec{E}_1^*(t_1) \\ \vec{E}_4^*(t_4) \cdot \vec{E}_2(t_2) \vec{E}_3(t_3) \cdot \vec{E}_1^*(t_1) \\ \vec{E}_4^*(t_4) \cdot \vec{E}_1^*(t_1) \vec{E}_3(t_3) \cdot \vec{E}_2(t_2) \end{bmatrix}.
\end{aligned} \tag{7}$$

It is clear from the above that by choosing the position of the detectors, we can selectively measure one of the three contributions to the four-wave mixing processes represented by Figs. (1.DQC.A, 1.NRP.SE & 1.PE.SE), along with their respective disconnected con-

tributions represented by the Figs. (2.DQC.A.DC<sub>1/2</sub>, 2.NRP.SE.DC & 2.PE.SE.DC). This has to be contrasted with the standard classical heterodyne detected signal, where a single pulse is detected. For temporally well separated pulses,  $\{\vec{E}_1(t), \dots, \vec{E}_4(t)\}$  this is given by,

$$\begin{aligned}
\mathcal{S}_{\mathcal{H}} = & -\frac{2}{\hbar^4} \text{Re} \int_{-\infty}^{+\infty} dt_4 \int_{-\infty}^{t_4} dt_3 \int_{-\infty}^{t_3} dt_2 \int_{-\infty}^{t_2} dt_1 \sum_{n_4, \dots, n_1=x,y,z} \\
& \Phi(\mathbf{k}_4 + \mathbf{k}_3 - \mathbf{k}_2 - \mathbf{k}_1) \times \\
& [\langle \mathcal{V}_L^{n_4}(t_4) \mathcal{V}_L^{n_3}(t_3) \mathcal{V}_L^{n_2\dagger}(t_2) \mathcal{V}_L^{n_1\dagger}(t_1) \rangle_s - \langle \mathcal{V}_L^{n_4}(t_4) \mathcal{V}_R^{n_3}(t_3) \mathcal{V}_L^{n_2\dagger}(t_2) \mathcal{V}_L^{n_1\dagger}(t_1) \rangle_s] \\
& \times \mathcal{R}_{n_4, n_3, n_2, n_1}^T \begin{bmatrix} \vec{E}_4^*(t_4) \cdot \vec{E}_3^*(t_3) \vec{E}_2(t_2) \cdot \vec{E}_1(t_1) \\ \vec{E}_4^*(t_4) \cdot \vec{E}_2(t_2) \vec{E}_3^*(t_3) \cdot \vec{E}_1(t_1) \\ \vec{E}_4^*(t_4) \cdot \vec{E}_1(t_1) \vec{E}_3^*(t_3) \cdot \vec{E}_2(t_2) \end{bmatrix} \\
& + \Phi(\mathbf{k}_4 - \mathbf{k}_3 + \mathbf{k}_2 - \mathbf{k}_1) \times \\
& [\langle \mathcal{V}_L^{n_4}(t_4) \mathcal{V}_R^{n_3\dagger}(t_3) \mathcal{V}_R^{n_2}(t_2) \mathcal{V}_L^{n_1\dagger}(t_1) \rangle_s - \langle \mathcal{V}_L^{n_4}(t_4) \mathcal{V}_L^{n_3\dagger}(t_3) \mathcal{V}_R^{n_2}(t_2) \mathcal{V}_L^{n_1\dagger}(t_1) \rangle_s + \langle \mathcal{V}_L^{n_4}(t_4) \mathcal{V}_L^{n_3\dagger}(t_3) \mathcal{V}_L^{n_2}(t_2) \mathcal{V}_L^{n_1\dagger}(t_1) \rangle_s] \\
& \times \mathcal{R}_{n_4, n_3, n_2, n_1}^T \begin{bmatrix} \vec{E}_4^*(t_4) \cdot \vec{E}_3(t_3) \vec{E}_2^*(t_2) \cdot \vec{E}_1(t_1) \\ \vec{E}_4^*(t_4) \cdot \vec{E}_2^*(t_2) \vec{E}_3(t_3) \cdot \vec{E}_1(t_1) \\ \vec{E}_4^*(t_4) \cdot \vec{E}_1(t_1) \vec{E}_3(t_3) \cdot \vec{E}_2^*(t_2) \end{bmatrix} \\
& + \Phi(\mathbf{k}_4 - \mathbf{k}_3 - \mathbf{k}_2 + \mathbf{k}_1) \times \\
& [\langle \mathcal{V}_L^{n_4}(t_4) \mathcal{V}_R^{n_3\dagger}(t_3) \mathcal{V}_L^{n_2\dagger}(t_2) \mathcal{V}_R^{n_1}(t_1) \rangle_s - \langle \mathcal{V}_L^{n_4}(t_4) \mathcal{V}_L^{n_3\dagger}(t_3) \mathcal{V}_L^{n_2\dagger}(t_2) \mathcal{V}_R^{n_1}(t_1) \rangle_s + \langle \mathcal{V}_L^{n_4}(t_4) \mathcal{V}_L^{n_3\dagger}(t_3) \mathcal{V}_R^{n_2\dagger}(t_2) \mathcal{V}_R^{n_1}(t_1) \rangle_s] \\
& \times \mathcal{R}_{n_4, n_3, n_2, n_1}^T \begin{bmatrix} \vec{E}_4^*(t_4) \cdot \vec{E}_3(t_3) \vec{E}_2(t_2) \cdot \vec{E}_1^*(t_1) \\ \vec{E}_4^*(t_4) \cdot \vec{E}_2(t_2) \vec{E}_3(t_3) \cdot \vec{E}_1^*(t_1) \\ \vec{E}_4^*(t_4) \cdot \vec{E}_1^*(t_1) \vec{E}_3(t_3) \cdot \vec{E}_2(t_2) \end{bmatrix}.
\end{aligned} \tag{8}$$

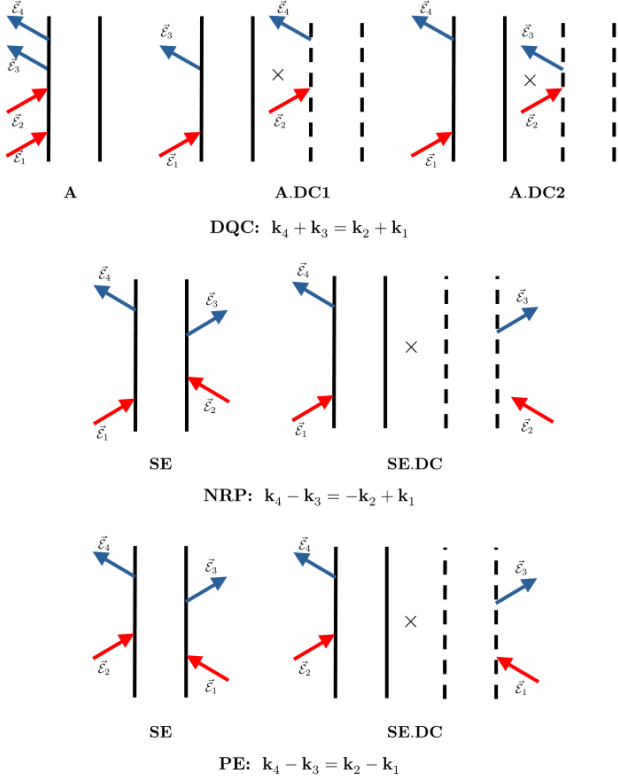


FIG. 2. Ladder diagrams contributing to the three dominant phase matching directions to the proposed coincident double heterodyne detected four-wave mixing signals.

For this signal, phase matching only selects the subclass of the ladder diagrams given in either of Figs. (1.DQC, 1.NRP & 1.PE). Hence measuring more than a single pulse, along with phase matching, gives additional pathway selectivity in our double heterodyne detection signal. In Ref. ([3]), an interferometric scheme employing entangled photons was proposed for selecting the diagram Figs. (1.DQC.A) in double quantum coherence spectroscopy.

### III. THE HIERARCHICAL EQUATIONS OF MOTION METHOD FOR COMPUTATION OF MULTIPOINT CORRELATION FUNCTIONS OF NON-MARKOVIAN OPEN QUANTUM SYSTEMS

Here we first provide a derivation of the Hierarchical Equations of Motion approach for simulating the dynamics and time-ordered multipoint correlation functions of non-markovian open quantum systems [4–6], with focus on the Frenkel dimer model.

The density matrix of the dimer in the presence of classical stochastic noise (modeling the environment-induced site energy fluctuations) evolves according to the equation

$$\frac{d}{dt}|\rho(t)\rangle\rangle = \mathcal{L}(t)|\rho(t)\rangle\rangle$$

$$\mathcal{L}(t) = -iH_- - i \sum_{n=1}^2 \eta_n(t) \left( B_{nL}^\dagger B_{nL} - B_{nR}^\dagger B_{nR} \right)$$

where  $h$  is the single exciton Hamiltonian.

The formal solution for the system density matrix is,

$$|\rho(t)\rangle\rangle = \mathcal{T} e^{-\int_{-\infty}^t d\tau \mathcal{L}(\tau)} |\rho(-\infty)\rangle\rangle, \quad (10)$$

which, in the interaction picture with respect to coupling to stochastic noise, is,

$$|\rho^I(t)\rangle\rangle = \mathcal{T} e^{-i \sum_{n=1}^2 \int_{-\infty}^t d\tau \eta_n(\tau) \mathbb{V}_{n-}(\tau)} |\rho(-\infty)\rangle\rangle, \quad (11)$$

where  $\mathbb{V}_{n-} = B_{nL}^\dagger B_{nL} - B_{nR}^\dagger B_{nR}$  and  $\mathcal{O}(\tau) = e^{iH_- \tau} \mathcal{O} e^{-iH_- \tau}$ . We are interested in computing the following correlation functions of the system,

$$\begin{aligned}
\mathcal{C}^{(n)}(t_1, \dots, t_n) &= \left\langle \left\langle \mathcal{I} | \mathcal{T} e^{-i \sum_{n=1}^2 \int_{-\infty}^t d\tau \eta_n(\tau) \mathbb{V}_{n-}(\tau)} \mathcal{O}_1(t_1) \cdots \mathcal{O}_n(t_n) | \rho(-\infty) \right\rangle \right\rangle_{\{\eta_n(\tau)\}} \\
\mathcal{O}_k(t_k) &= \mathcal{V}_{n_k \sigma}(t_k) / \mathcal{V}_{n_k \sigma}^\dagger(t_k) \quad (n_k = x, y, z \text{ \& } \sigma = L, R) \\
\vec{\mathcal{V}} &= \sum_{n=1}^2 \vec{\mu}_n B_n,
\end{aligned} \tag{12}$$

where  $\langle \cdots \rangle_{\{\eta_n(\tau)\}}$  stands for averaging over classical stochastic Gaussian coloured noise, with zero mean and variance given by  $\langle \eta_m(t) \eta_n(t') \rangle = \delta_{mn} \alpha_n^2 e^{-\gamma_n |t-t'|}$ . To

wards this goal, we introduce the generating function and the modified density matrix, respectively as,

$$\mathcal{Z}[\{\vec{\Upsilon}_\sigma(\tau)\}] = \langle \langle \mathcal{I} | \rho_{\vec{\Upsilon}}^I(+\infty) \rangle \rangle \tag{13}$$

$$|\rho_{\vec{\Upsilon}}^I(t)\rangle\rangle = \left\langle \left\langle \mathcal{T} e^{-\int_{-\infty}^t d\tau \left( -i \sum_{n=1}^2 \eta_n(\tau) \mathbb{V}_{n-}(\tau) - i \sum_{\sigma=L,R} [\vec{\Upsilon}_\sigma^\dagger(\tau) \cdot \vec{\mathcal{V}}_\sigma(\tau) + \vec{\mathcal{V}}_\sigma^\dagger(\tau) \cdot \vec{\Upsilon}_\sigma(\tau)] \right)} \right\rangle \right\rangle_{\{\eta_n(\tau)\}} |\rho(-\infty)\rangle\rangle. \tag{14}$$

Functional derivatives of  $\mathcal{Z}[\{\vec{\Upsilon}_\sigma(\tau)\}]$  at  $\{\vec{\Upsilon}_\sigma(\tau)\} = \{0\}$  give the desired correlation functions. Note that here  $\vec{\Upsilon}_R(\tau) \neq -\vec{\Upsilon}_L(\tau)$ . The average modified density matrix

of the dimer, obtained after performing noise averaging, is given by,

$$|\rho_{\vec{\Upsilon}}^I(t)\rangle\rangle = \mathcal{T} e^{-\int_{-\infty}^t d\tau \left( -i \sum_{\sigma=L,R} [\vec{\Upsilon}_\sigma^\dagger(\tau) \cdot \vec{\mathcal{V}}_\sigma(\tau) + \vec{\mathcal{V}}_\sigma^\dagger(\tau) \cdot \vec{\Upsilon}_\sigma(\tau)] - \sum_{n=1}^2 \alpha_n^2 \mathbb{V}_{n-}(\tau) \int_{-\infty}^{\tau} d\tau' e^{-\gamma_n(\tau-\tau')} \mathbb{V}_{n-}(\tau') \right)} |\rho(-\infty)\rangle\rangle. \tag{15}$$

The time non-local propagator in the above equation is commonly referred to as the influence functional. One standard way to handle this non-markovian evolution is by deriving an infinite tower of coupled equations called Hierarchical Equations of Motion. This infinite

tower of equations can be conveniently recast by introducing auxiliary oscillators (bosons). Here, we arrive at these equations in a slightly different way. We decouple the non-markovian evolution given above by a Hubbard-Stratanovich transformation using the identity,

$$\mathcal{T} e^{-\sum_{n=1}^2 \int_{-\infty}^t d\tau \int_{-\infty}^{\tau} d\tau' \mathcal{O}_n(\tau) e^{-\gamma_n(\tau-\tau')} \mathcal{O}_n(\tau')} = \langle 0, 0 | e^{\sum_{n=1}^2 \int_{-\infty}^t d\tau [-\gamma_n a_n^\dagger a_n - i \mathcal{O}_n(\tau) (a_n^\dagger + a_n)]} | 0, 0 \rangle, \tag{16}$$

where  $|0, 0\rangle$  is the vacuum concerning the auxiliary

bosons described by the annihilation operators  $\{a_1, a_2\}$ . This gives,

$$\begin{aligned}
|\rho_{\vec{\Upsilon}}(t)\rangle\rangle &= \langle 0, 0 | \check{\rho}_{\vec{\Upsilon}}(t) \rangle\rangle \\
|\check{\rho}_{\vec{\Upsilon}}(t)\rangle\rangle &= e^{-\int_{-\infty}^t d\tau \left( -iH - \sum_{n=1}^2 \gamma_n a_n^\dagger a_n - i \sum_{n=1}^2 \alpha_n \mathbb{V}_{n-} (a_n^\dagger + a_n) - i \sum_{\sigma=L,R} [\vec{\Upsilon}_\sigma^\dagger(\tau) \cdot \vec{\mathcal{V}}_\sigma + \vec{\mathcal{V}}_\sigma^\dagger \cdot \vec{\Upsilon}_\sigma(\tau)] \right)} |\check{\rho}(-\infty)\rangle\rangle,
\end{aligned} \tag{17}$$

where in the second line, we introduced the joint modified density operator for the dimer and the auxiliary bosons and  $|\check{\rho}(-\infty)\rangle\rangle = |\rho(-\infty)\rangle\rangle \otimes |0, 0\rangle$ . Note that the above equation is written in the Schrodinger picture. Standard scaled Hierarchical Equations of motion are now equivalent to the infinite tower of coupled equations for

$$\begin{aligned} \mathcal{Z}[\{\check{\Upsilon}_\sigma(\tau)\}] &= \langle\langle \mathcal{I} | \otimes \langle 0, 0 | e^{-\int_{-\infty}^t d\tau \left( \check{L} - i \sum_{\sigma=L,R} [\check{\Upsilon}_\sigma^\dagger(\tau) \cdot \check{\mathcal{V}}_\sigma + \check{\mathcal{V}}_\sigma^\dagger \cdot \check{\Upsilon}_\sigma(\tau)] \right)} | \rho(-\infty)\rangle\rangle \otimes |0, 0\rangle \\ \check{L} &= -iH_- - \sum_{n=1}^2 \gamma_n a_n^\dagger a_n - i \sum_{n=1}^2 \alpha_n \mathbb{V}_{n-} (a_n^\dagger + a_n). \end{aligned} \quad (18)$$

It is useful to note that  $\langle\langle \mathcal{I} | \otimes \langle 0, 0 | \check{L} = 0$ . Finally, by taking the functional derivatives of the generating func-

$\langle m, n | \rho_{\check{\Upsilon}}(t) \rangle\rangle$ , the partial projections of the joint density matrix on to the occupation number basis of auxiliary bosons. Specifically, the physical density matrix is given by  $\langle 0, 0 | \rho_{\check{\Upsilon}=0}(t) \rangle\rangle$ .

Finally, the generating function for the dimer correlation functions is given as,

tion with respect to the source at zero sources gives the following correlation function for a specific time order,

$$\begin{aligned} \mathcal{C}_{k_1, \dots, k_n}^{(n)}(t_1, \dots, t_n) &\equiv \left\langle \left\langle \mathcal{I} | \mathcal{T} e^{-i \sum_{n=1}^2 \int_{-\infty}^t d\tau \eta_n(\tau) \mathbb{V}_{n-}(\tau)} \mathcal{V}_1^{k_1}(t_1) \dots \mathcal{V}_n^{k_n}(t_n) | \rho(-\infty)\rangle\rangle \right\rangle_{\{\eta_n(\tau)\}} \\ &\stackrel{t_n > \dots > t_1}{=} \langle\langle \mathcal{I} | \otimes \langle 0, 0 | \mathcal{V}_n^{k_n} \check{\mathcal{G}}(t_n - t_{n-1}) \dots \mathcal{V}_2^{k_2} \check{\mathcal{G}}(t_2 - t_1) \mathcal{V}_1^{k_1} | \check{\rho}(\infty)\rangle\rangle \text{ with } \check{\mathcal{G}}(t) = e^{\check{L}t}. \end{aligned} \quad (19)$$

Here to arrive at the last line, we used  $\langle\langle \mathcal{I} | \otimes \langle 0, 0 | \check{L} = 0$  and the steady state  $|\check{\rho}(\infty)\rangle\rangle = \lim_{t \rightarrow \infty} \check{\mathcal{G}}(t) |g\rangle\langle g| \otimes |0, 0\rangle$ , where  $|g\rangle$  is the ground state of  $H$ . Numerical

computations are performed in the Hilbert space basis  $\{|N_{1l}, N_{2l}\rangle\langle N_{1r}, N_{2r}|\} \otimes |n_1, n_2\rangle : N_{1l}, N_{2l}, N_{1r}, N_{2r} \in \{0, 1\} \ \& \ n_1, n_2 \in \mathbb{N} \ \& \ n_1 + n_2 \leq n_{cut}\}$  with  $n_{cut} = 10$ .

- [1] K. E. Dorfman, F. Schlawin, and S. Mukamel, Nonlinear optical signals and spectroscopy with quantum light, *Rev. Mod. Phys.* **88**, 045008 (2016).
- [2] D. L. Andrews and T. Thirunamachandran, On three-dimensional rotational averages, *J. Chem. Phys.* **67**, 5026 (1977).
- [3] M. Kizmann, H. K. Yadalam, V. Y. Chernyak, and S. Mukamel, Quantum interferometry and pathway selectivity in the nonlinear response of photosynthetic excitons, *Proc. Natl. Acad. Sci.* **120**, e2304737120 (2023).

- [4] Y. Tanimura and S. Mukamel, Real-time path-integral approach to quantum coherence and dephasing in nonadiabatic transitions and nonlinear optical response, *Phys. Rev. E* **47**, 118 (1993).
- [5] Y. Tanimura, Stochastic liouville, langevin, fokker-planck, and master equation approaches to quantum dissipative systems, *J. Phys. Soc. Japan* **75**, 082001 (2006).
- [6] Y. Tanimura, Numerically “exact” approach to open quantum dynamics: The hierarchical equations of motion (heom), *J. Chem. Phys.* **153** (2020).